NTNU

Norwegian University of
Science and Technology

A K-Space Filtering Technique for Vibration Sonoelastography

Mikkel Øyvind Henninen

Master of Science in Cybernetics and Robotics
Submission date: June 2016
Supervisor: Hans Torp, ITK
Co-supervisor: Alfonso Rodriguez-Molares, Institutt for sirkulasjon og bildediagnostikk

Norwegian University of Science and Technology
Department of Engineering Cybernetics

A k-space filtering technique for vibration sonoelastography

Mikkel Henninen

June 2016

MASTER THESIS

Department of Engineering Cybernetics

Norwegian University of Science and Technology

Supervisors: Alfonso Rodriguez-Molares and Hans Torp

Preface

This report is the conclusion of my masters degree in Technical Cybernetics at the Norwegian University of Science and Technology (NTNU). The work has been done at the Department of Circulation and Medical Imaging (ISB) of the Faculty of Medicine (DMF) of NTNU, and was supervised by Professor Hans Torp from ISB and co-supervised by Post Doc and Senior engineer Alfonso Rodriguez-Molares from ISB. The project was done during the spring semester of 2016.

Acknowledgment

First I would like to thank my day to day supervisor, Alfonso Rodriguez-Molares, for being the giant whose shoulders I've stood upon. Without him, I would neither have thought about doing this project, nor managed to finish it. His availability and quick responses has made this semester a lot easier, and his quick wit has made it very enjoyable as well.

Secondly I would like to thank all those who have helped me proofread and edit my thesis: Bjørn, Kristin, Beate and Hans, you raised my thesis to a way better level.

Finally I would like to thank Britt Unni Haukvik, my girlfriend, for accepting my complete absentmindedness during the course of this project, for helping me focus when I wanted to procrastinate and for generally being here with me throughout this endeavour.

Trondheim, 06/06-2016

Mikkel Henninen

Sammendrag

Dette prosjektets mål var å undersøke hvorvidt det er mulig å beregne elastisiteten til et medium ved bruk av stasjonære vibrasjonsfelt og filtrering i et frekvensplan nådd ved bruk av en 2D Fourier transformasjon. Metoden ble implementert i MATLAB og testet mot numerisk og eksperimentell data innhentet fra et avbildningsfantom.

Metoden klarer ikke å gjenkjenne størrelse eller posisjon på en eventuelt svulst ved lavere frekvens enn 1000 Hz, verken i eksperimentell eller numerisk data. I numerisk data ved 2500 Hz klarte metoden å ekstrahere både bølgehastighet i svulsten og dens posisjon og størrelse. Resultatene våre indikerer at en slik filtrering i frekvensplanet kan fungere for å oppdage brystkreft ved høyere frekvenser, men videre arbeid er nødvendig. For det første trenger metoden å forbedres med en sterkere vibrasjonskilde. I tillegg må en 3D-innhenting av data brukes for å unngå bølger som går på skrått av innhentingsplanet ved 2D innhenting. Til slutt anbefales det å implementere et automatisk aktiveringssystem for å unngå ubehag både for pasient og medisinsk personell.

Abstract

The aim of this project was to investigate the feasibility of a k-space filtration technique to produce elasticity maps with stationary vibration fields. The method was implemented in a MATLAB routine and tested against numerical and experimental data gathered from an imaging phantom.

The method is unable to correctly detect the cyst at frequencies less than 1000 Hz, both in experimental and numerical data. With numerical data at 2500 Hz the method successfully extracts both the speed and the shape of the cyst. Our results indicate that, while the k-filtering approach might be feasible for detection of breast cancer at high frequency, further work is needed. Primarily a more powerful source of vibration must be used. Secondly a 3D acquisition scheme must be used to deal with transversal vibration modes. Finally, gated operation is recommended to reduce discomfort for both patient and operator.

Abbreviations and frequently used symbols

Abbreviations

NTNU Norwegian University of Science and Technology

ISB Department of Circulation and Medical Imaging

DMF Faculty of Medicine

MRI Magnetic Resonance Imaging

CT Computed Tomography

US Ultrasonography

SWE Shear Wave Elastography

SSI Supersonic Shear Imaging

TE Transient Elastography

VA Vibro-acoustography

ARFI Acoustic Radiation Force Impulse

USTB Ultrasound Toolbox

PWI Plane-Wave Imaging

PRF Pulse Repetition Frequency

TDI Tissue Doppler Imaging

PVA Poly-Vinyl Alcohol

FT-Cycles Freeze-Thaw Cycles

FEM Finite Element Method

Frequently used symbols

c Speed of longitudinal waves in m/s

ρ Density in kg/m^3

c_s Speed of shear waves in m/s

G shear modulus in N/m^2

f_0 Excitation frequency in Hz

k Wavenumber in rad/m, k_x and k_z are components of k

λ Wavelength in m

Contents

Chapter 1

Introduction

This chapter introduces the problem at hand, the aim of the project and its limitations. It also presents a short background on the history of ultrasound and elastography as well as why and how it is used today.

1.1 Problem statement

This project investigates a novel analysis method for vibration sonoelastography by k-space filtration. The method proposed in this thesis could in theory be faster, more precise and have a better penetration than the state-of-the-art methods.

Through better detection of tumors, both the number of false positives and the number of false negatives can be reduced. Reducing the number of false positives would ensure that less people has to go through unneeded medical treatment and the stress that follows believing you have cancer. Reducing the number of false negatives means that cancer is detected earlier, which reduces the extent and spread of the condition. Ultimately, this would reduce both costs in medical treatment as well as reducing the morbidity and mortality of cancer.

1.2 Objectives

The main objectives of this project are

1. To investigate the feasibility of a k-space filtering technique to vibration sonoelastography.
2. Assess its accuracy, validity and clinical feasibility.
3. Design and produce PVA cryogel phantoms for elastography testing.
4. Design an experimental setup to induce vibration fields.

1.3 Limitations

As this method is novel and untested, it would not be approved for a clinical trial if we were to apply for one. Clinical trials require experimental proof that the method works before you are allowed to test it on humans. This mean that the proposed method will only be tested on phantoms and numerical data, not live test subjects. The results from this project will thus only be an indication of how well the method can work. A proper clinical trial would be needed to assess the method.

1.4 Breast cancer

Breast cancer is the most common form of cancer among women, and its incidence is increasing. The incidence has had a steady incline from 37.6 per 100 000 women in the time span 1955-1959 to 77.4 per 100 000 women in 2010-2014. While it is not as prevalent among men, in the same time frame the rate has increased from 0.3 per 100 000 to 0.6 per 100 000 [1]. This trend has no singular reason, but amongst others, lifestyle and better screening can be major causes [2]. Norway has a very extensive screening program for breast cancer of women, which started in 1995 and by the end of 2005 it reached its goal of offering all women between 50 and 69 years old a screening [3]. According to the Cancer Registry of Norway the incidence of breast cancer has at least doubled after the screening program started [2]. In Norway breast cancer had a mortality rate of 12% for women in the period 2010-2014. In total 663 women and 6 men died from breast cancer that year.

1.5 Ultrasound

Ever since humans started having a tenuous grasp on medicine, palpation has had a vital role in diagnosis. In China there has been found references to palpation in diagnosis dating back to 475 - 221 B.C. [4], and in Egypt the technique was ascribed to Imhotep, an architect, priest and physician who lived around 2500-3000BC [5]. It is "the act of feeling with the hand" [6]. By feeling or pushing on an abnormality under the skin a trained examiner can estimate its size, firmness and shape. This has been an important tool for diagnosis because many medical conditions change the mechanical properties of the affected tissue, e.g cancerous tumors are stiffer than the surrounding tissue. Palpation is limited by how deeply you are able to probe with your fingers and how sensitive your fingers are. This means that deep and small abnormalities would go undetected. Palpation is also a subjective technique that requires extensive training, which is a major disadvantage. In the last century medical technology has brought new solutions to this problem. Methods such as Magnetic Resonance Imaging (MRI), Computed Tomography (CT) and Ultrasonography (US) can be used to map the stiffness of the body and detect different kinds of abnormalities. While both MRI and CT provides reliable images, mainly due to their superior image contrast, both techniques are costly, non-portable and, in the case of CT, hazardous. Ultrasonography, on the other hand, is cheap, portable and harmless as long as it is used within well-established safety limits. By using ultrasound changes in acoustic impedance are mapped in order to generate an internal image of the body. Regions containing bone, air or gas are opaque to ultrasound transducers, which makes US not viable for brain and lung imaging [7]. CT and MRI creates superb images of the brain, bone and lung tissue, so they are complementary to ultrasound.

1.6 The birth of ultrasound

Ultrasound is like regular sound, only at higher frequency. What is considered audible sound for humans are pressure waves ranging from 20 to 20 000 Hz, and ultrasound refers to the waves above that frequency. Contrary to audible sound, ultrasound can be used to remotely extract spatial information with great precision. Some animals, like bats, use this property both to navigate the world and locate prey. Humans, on the other hand, only started using ultrasound in the

beginning of the 20th century. Just a few months after the Titanic sank in 1912, the first patent regarding ultrasound was filed: a system to detect submerged icebergs with ranged ultrasound, which could have been used to prevent the famous tragedy. This patent was the precursor of the Sound Navigation and Ranging, a technology widely known by its acronym SONAR. Due to scientific breakthroughs both in hardware manufacturing and theoretical fields in the 40s and 50s, SONAR-technology was adapted to medical diagnosis. In 1941 Karl Theo Dussik, an Austrian neurologist, applied transmission ultrasound to outline the ventricles of the brain. Unfortunately, the complicated physical properties of the cranium foiled his work. In 1953, Dr. I. Edler and Professor C. H. Hertz (the nephew of the very Hertz whose name is the origin of the unit), used ultrasound to detect Hertz's heart motions, and thus echocardiography was born [8].

Ultrasound technology has evolved rapidly in the years since Hertz and Edler worked with it. Different imaging modalities and data filtering techniques as well as better hardware lets us use ultrasound to detect abnormalities in almost any part of the body, like heart [9], liver [10] or bones [11]. It is also possible to produce images in 3D due to better image processing and raw computer power [12]. The technology has also managed to decrease in size, all the way down to handheld equipment weighing less than half a kilogram [13], increasing both practicality and removing logistics issues.

1.7 Sonoelastography

Instead of palpation, an ultrasound probe can be used to find abnormalities in the body (for instance cancerous tumors) of a wide range of depths and sizes. While ultrasound shows the changes in acoustic impedance of the inspected tissue, it does not give any direct information about the stiffness of the tissue. Certain abnormalities, like tumors and cirrhotic tissue, has very similar acoustic impedance to regular tissue [7], and thus may not be seen in regular ultrasound imaging. However, those abnormalities can have a different stiffness than regular tissue, and could be found by mapping the tissue stiffness. This can be done with US by perturbing the tissue with a mechanical wave and tracking the tissue displacement. As the amplitude of the

displacement will be smaller in stiffer regions than in the less stiff regions, the displacement can be used as a measure of stiffness. This is the basis for elastography.

Elastography was discovered when researching tissue motion back in the 80s. Using a modified color Doppler-method to track movement of the tissue, researchers at the University of Rochester found that they could estimate tissue stiffness [14]. Stiffer masses in the tissue would move less than the surrounding tissue, and thus would be displayed as darker areas. The technique had low resolution, but was able to find masses in the body that regular ultrasound could not find. The technique was further improved by Cespedes and Ophir in 1991 by using the probe to push and deform the tissue underneath, tracking the resulting distortions, and finding relative tissue stiffness [15]. This "strain-elastography" was successfully used to classify breast masses as benign or malignant. Further developments lead to shear wave elastography (SWE); a method that uses shear waves to get a map of the shear and elastic moduli of the tissue [16].

Different methods of elasticity imaging has been developed in the last 30 years. The most widely used nowadays is acoustic radiation force impulse (ARFI) imaging. ARFI uses focused ultrasound to excite the tissue and generate a transitory mechanical excitation. This impulse produces a shear wave that propagates through the tissue. The propagating wave is tracked using Doppler ultrasound and its velocity is estimated. From the shear wave velocity the tissue stiffness is extracted. Methods based on ARFI have been implemented in most commercial scanners by companies like GE Healthcare [17], Siemens [18], Phillips [19] and SuperSonic Imagine [20]. ARFI has limitations with attenuation and low frame rate. While the attenuation issues could be addressed by Comb-Pushing [21], it decreases the frame rate further [22].

An extension of ARFI is supersonic shear imaging (SSI). By moving the focal point of ARFI faster than the shear waves move, a constructive interference occurs, changing the wave pattern into a conical shear wave. It requires a scanner capable of 5000 frames/s or higher, but it is also faster and thus less affected by patient movement. It has been used in assessment of phantoms, liver, breast and skeletal muscle [23], [24] and [25].

Another method developed is transient elastography (TE). In transient elastography, an external actuator is used to provide a single cycle of low-frequency vibration. Ultrasound is used to track the motion. This generates shear- and compressional waves in the medium. As the compressional wave is faster than the shear wave in most cases, they are separated in time. The temporal difference can be found using cross-correlation, and this time shift estimate can determine how much motion has occurred. TE has successfully been used to measure stiffness of the liver in FibroScan®made by EchoSens [26]. It has also been used to measure stiffness in blood clots [27], phantoms [28] and breasts [29].

Vibro-acoustography (VA) is another method in development. It uses excitations caused by concentrating two separate ultrasound beams at high and slightly different frequencies in a point. This results in a stationary vibration field in the tissue, which is measured using a hydrophone. The amplitudes of the field are recorded and used to make an elasticity map of the region. In 2002 VA was successfully used to detect breast lesions *ex vivo* [30] and in 2004 it was tested on 74 tissue samples and proven to be able to detect 78.4% of the microcalcifications, which can be an indicator of cancer [31]. In 2005 VA was tested *in vivo* [32]. In 2006 a VA system was intergrated in a clinical stereotactic mammography machine, combining X-ray and VA imaging in one machine [33], and in 2007 the system was shown to produce images with a registration error of less than 1.65mm [34]. All of these articles state that VA may have issues with computation time, resolution and tissue attenuation. VA also struggles with the reflections that arise when the waves hit an interface.

1.8 Structure of the report

Chapter 2 presents the theory that supports the method as well as all the theory needed to carry this investigation. It also presents the investigation hypothesis. Chapter 3 presents the material and methods used to verify the hypothesis. In Chapter 4 the results will be presented, and Chapter 5 will contain a discussion of the results. Finally, Chapter 6 will conclude the report and give suggestions for further work.

Chapter 2

Theory

This chapter will introduce the k-space filtering approach for vibration sonoelastography. It will explain the different data processing steps used in the proposed method, and how it works.

2.1 Ultrasonography

Ultrasonography is a medical diagnostic technique that works by sending high frequency acoustic waves into the body. This is done using piezoelectric materials. Piezoelectricity is a two-way process that either converts mechanical energy into electricity or causes the material to vibrate when electricity is applied [35]. Many materials exhibit piezoelectricity: crystals like sucrose and quarts, tendons, silk and others. Piezoelectric materials are used in ultrasound probes as transducers: both generators and sensors [7].

Regular ultrasound uses longitudinal waves, also called pressure waves. In longitudinal waves the displacement happens in the direction of propagation. When the ultrasonic waves encounter a change in the medium acoustic impedance, a part of the wave will be reflected back towards the probe. An estimate of how deep the wave went before it got reflected can be found by measuring the time-of-flight. This works because the speed of sound is relatively constant in soft tissues at c =1540 m/s, which gives the relation

$$d = \frac{ct}{2} \tag{2.1}$$

where c is the wave speed in m/s, t is the round trip time in s, and d is the depth of the source of reflection in m. The amplitude of the reflected wave can be extracted from the reflection coefficient

$$RF = \frac{Z_2 - Z_1}{Z_1 + Z_2} \tag{2.2}$$

where Z_1 is the impedance of the original medium and Z_2 is the impedance of the new medium the wave reaches, both given in kg/sm^2. This formula shows that the bigger the change in impedance, the more energy is reflected.

The simplest method of medical ultrasound is the amplitude mode, or A-mode, which is the mapping of (2.1) to (2.2) along a single scanning line. This measurement is often repeated at consecutive points in time, creating a 2D image showing the temporal evolution of the scanline. From this A-mode image doctors can study the movement of body organs, and extract both velocities and displacements. A more complex method is achieved by moving the scanning line to sweep a 2D area. This results in a 2D image of the body structures known as brightness mode, or B-mode, image. Typically a ultrasound probe will consist of an array of several piezoelectric transducers. By actuating on the signals emitted by each individual transducer we manipulate the spatial wavefront of the transmitted wave, making it possible for instance to focus the beam on specific points or cover wider areas with plane-waves. This method, called beamforming, can be also applied on receive to achieve dynamic focusing and optimal resolution [7].

Ultrasound is mostly in soft biological tissues due to the poor penetration of ultrasound in hard tissue. While soft tissues are solids, they can be modeled as fluids without much loss of accuracy [36]. There are two major properties governing the waves in the tissue: elasticity (compressibility, κ, in m^2/N) and inertia (density, ρ, in kg/m^3). Other relevant properties can be derived from these two, like wave speed:

$$c = \sqrt{\frac{1}{\kappa\rho}}. \tag{2.3}$$

Biological tissue is not homogeneous, which results in energy loss as the wave travels through the medium. When a wave travels through any medium, some of the vibrational energy is transferred to the medium as heat, which is called absorption [36]. Every time the wave hits any small change in impedance, like a small pocket of fat, some of the energy will be reflected. When the wave reaches a change in the body, for instance an internal organ, the reflection can either be specular or diffuse. Specular reflections are reflections that travel only in one direction. They are caused by flat and smooth interfaces and are normally caused at wavelengths shorter than the reflecting structure. They can easily be seen in the ultrasound output. Diffuse reflections, or scattering, occurs when the interface is non-smooth, and consists of many smaller reflections in several directions. They are normally caused by ultrasound wavelengths that are larger than the reflecting structure [37]. All of these effects cause the energy of the original signal to fall both as a function of depth of imaging and frequency. The sum of these effects is called attenuation.

2.2 Sonoelastography

Elastography can be used to extract more information than by regular ultrasound. It is done in three steps: creating a mechanical excitation, estimating the tissue deformation caused by the excitation, and post processing of the data. The excitation can be produced in several ways, the most common ones being [38]:

1. By using an external source, like a mechanical shaker or even just pushing with your hand.

2. By focusing the ultrasonic beam on a region for a prolonged time, making the radiation force induce an excitation at the focal area.

3. By using the internal forces in the body like the pulse or heartbeat.

Tissue deformation is then observed by the imaging method, in our case ultrasound. The tissue deformation data can then be used to estimate the elastic properties of the tissue. This

estimation depends on how the deformation was caused. If the excitation is a static, or quasi-static, pressure the stress-strain-relationship (stiffer materials deform less) can be used. However, one usually does not know exactly how big the stress will be inside the body, and thus can only estimate the strain on a relative scale [38]. If the excitation is dynamic, the relationship between the speed of the waves and the tissue stiffness can be used (waves travel faster through stiffer materials). This method does not require to know the stress within the tissue, and hence produces a quantitative estimation of the tissue stiffness.

Shear wave elastography (SWE) is a dynamic method. By inducing a time-varying mechanical perturbation, both compressional and shear waves are generated in a solid body [38]. Shear waves are transverse waves, their motion is perpendicular to the wave propagation, unlike longitudinal waves, where the motion is in the direction of propagation, as illustrated in Figure 2.1. The velocity of shear waves is given by the formula

$$c_s = \sqrt{\frac{G}{\rho}}, \tag{2.4}$$

where G is the shear modulus of the medium in $\mathrm{N/m^2}$. The shear modulus is also given by the quotient of shear stress divided by shear strain [39], that is the relative deformation as a function of pressure, which is a measure of the hardness of an object. The speed of shear waves in tissue is usually on the scale of 1-50 m/s [38], and it is higher the harder the tissue is. Equation (2.4) can be rewritten to

$$G = \rho c_s^2, \tag{2.5}$$

showing that the shear modulus, or hardness, is proportional to the density and the square of the shear wave speed.

2.3 Data processing methods

This section contains the theory of the following methods:

1. Beamforming

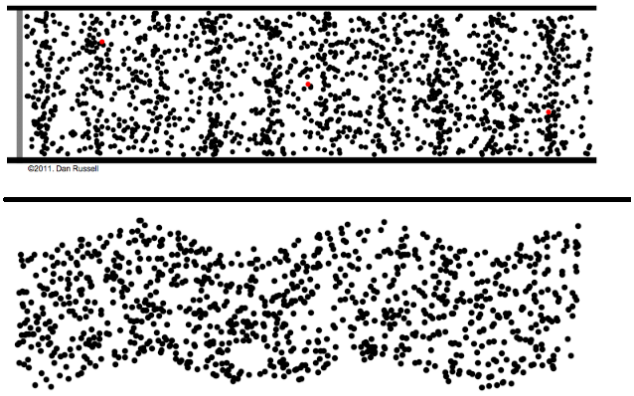

Figure 2.1: An illustration of longitudinal waves (top) and shear waves (bottom), taken from [40]

2. Tissue doppler imaging
3. K-space transformation
4. Frequency spectrum
5. Filtering
6. Cumulative velocity field

2.3.1 Beamforming

Beamforming converts the signals received by each element in the array into an spatial representation of the tissue under study. In the project this was done using the ultrasound toolbox (USTB) developed at ISB. The method implemented is plane-wave imaging (PWI), meaning that a (quasi)plane wavefront is produced, exciting the whole region of interest with one wavefront. In PWI the signal at the pixel (x,z) is computed as:

$$s(x,z) = \sum_{m=1}^{M} u_m h_m \left(\frac{z}{c_0} + \frac{D_m}{c_0} \right), \tag{2.6}$$

where M is the number of elements (or channels) in the array, u_m denotes the weighting value used with channel m corresponding to the receive aperture, $h_m(t)$ is the temporal signal received by channel m, and D_m is the distance between the pixel (x,z) and the element m [41]. An example of beamformed data showing a cyst can be seen in Figure 2.2.

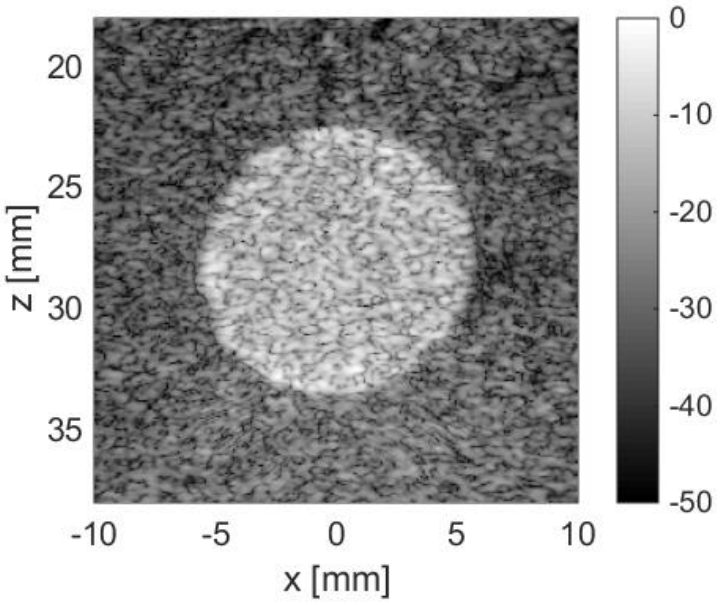

Figure 2.2: An example of beamformed data showing a cyst

2.3.2 Tissue Doppler Imaging

Most people have experienced the Doppler effect. When a car drives towards you, it sounds different than when it goes away from you, even more so when it is an ambulance with its sirens on. When interpreting audible sound, the main property we perceive is the frequency: how many beats reach our ears each second. When the car moves towards us, the distance between the consecutive beats will be lessened by the movement of the car, when the car drives away, the consecutive beats will be farther away and we perceive a lower frequency. An illustration of the phenomenon is shown in Figure 2.3. The perceived frequency for the observer can be calculated by

$$f_d = f_0 \frac{c}{c+v}, \tag{2.7}$$

where f_d is the frequency the observer perceives in Hz, f_0 is the frequency the source emits, c is the speed of sound in m/s and v is the speed of the source in m/s, defined as positive when the movement is away from the observer. Similarly, if it is the observer that is moving with velocity v and the source is still, there will be a shift in perceived frequency given by

$$f_d = f_0 \frac{c+v}{c}, \tag{2.8}$$

where v is the speed of the observer in m/s, defined as positive when the movement is towards the source. For further details the reader is referred to "University Physics" by Young, Freedman and Ford [42].

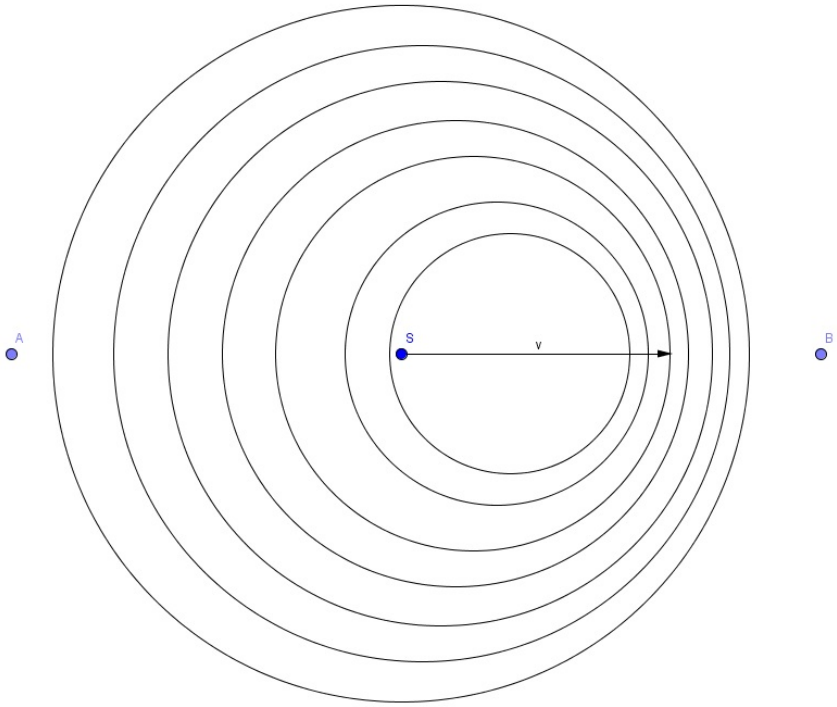

Figure 2.3: Doppler shifted frequencies as observed by an observer A behind the source and B ahead of the source

Local inhomogeneities in biological tissue produce an interference pattern referred to as speckle. When an ultrasonic wave hits a moving inhomogeneity, the speckle can be considered a moving observer and thus will "perceive" a doppler shift. The following reflection from the speckle will have a frequency given by equation (2.8), but now, as the speckle is the source of the reflection, while the probe is now an observer of the reflection, another doppler shift will occur, given by equation (2.7), with f_0 given by equation (2.8), giving a total doppler shift perceived by the probe of

$$f_d = f_0 \frac{c+v}{c-v}, \tag{2.9}$$

with v being the velocity of the speckle in m/s, defined as positive when the movement is towards the probe [42].

In 1985, C. Kasai et al. [43] showed that an estimate of the doppler frequency in pulsed doppler mode can be found by the following equation

$$f_D = \frac{\angle R_1 \, PRF}{2\pi}, \tag{2.10}$$

where $\angle R_1$ is the phase of the autocorrelation with lag 1, between consecutive pulses and PRF (Pulse Repetition Frequency) which describes how many pulses are sent per second. Then the tissue velocity can be found using the following equation:

$$v = \frac{f_D}{f_0} \frac{c}{2\cos\theta} \tag{2.11}$$

where θ is the angle between the direction of the ultrasonic beam and the direction of the velocity vector of the source of the reflection. The angle θ is assumed to be zero, meaning we measure the axial component of the velocity. Combining equations (2.10) and (2.11) and the assumption, we get

$$v = \frac{\angle R_1 \, PRF c}{4\pi f_0}. \tag{2.12}$$

This method of calculating a velocity map is an application of tissue doppler imaging (TDI). In our method equation (2.12) was implemented. Figure 2.4 shows a frame of how the data looks after beamforming on the left-hand side and how that frame looks after estimation of the tissue velocity on the right-hand side.

2.3.3 k-space

The Fourier-series describes how any function can be written as the sum of a set of sines with different amplitudes, phases and frequencies. An extension of this is the Fourier Transform,

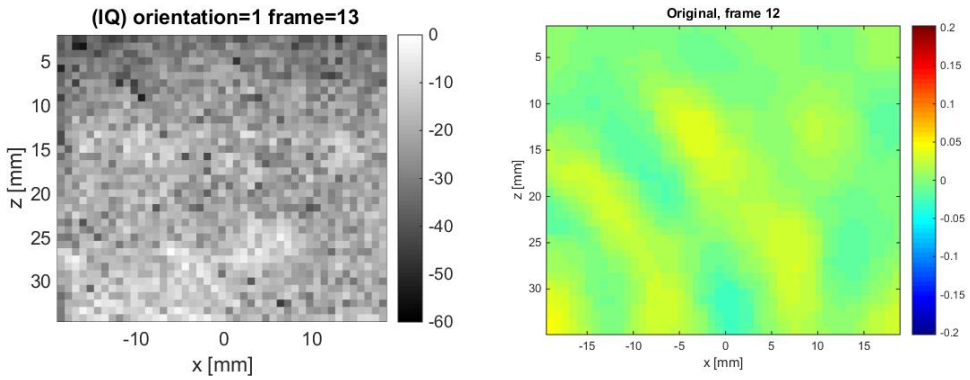

Figure 2.4: A frame of beamformed data (left) and a frame of the velocity field calculated by Tisssue Doppler Imaging

which transforms a signal into its frequency components. In some cases it is easier to analyze data in the frequency domain than in the spatial domain. Any spatial signal can be expressed in the frequency domain with the Fourier transform

$$F(k_x) = \int_{-\infty}^{\infty} f(x) e^{-ik_x x} \, \mathrm{d}x \tag{2.13}$$

and with the inverse of the Fourier transform given by

$$f(x) = \int_{-\infty}^{\infty} F(k_x) e^{ik_x x} \, \mathrm{d}k_x. \tag{2.14}$$

For both these equations, k_x represents the wavenumber in the x-axis, which is measured in rad/m, and i is the imaginary number $\sqrt{-1}$. The wavenumber can be expressed in terms of the spatial frequency as

$$k = 2\pi\xi. \tag{2.15}$$

Similarly, a 2D-picture can be decomposed into the frequency domain (and back again) by the 2D-Fourier transform pair, which is also called the k-space transform:

$$F(k_x, k_z) = \int_{-\infty}^{\infty} \int_{-\infty}^{\infty} f(x, z) e^{-i(k_x x + k_z z)} \, \mathrm{d}x \mathrm{d}y \tag{2.16}$$

$$f(x, z) = \int_{-\infty}^{\infty} \int_{-\infty}^{\infty} F(k_x, k_z) e^{i(k_x x + k_z z)} \, \mathrm{d}k_x \mathrm{d}k_z, \tag{2.17}$$

where f(x,z) is the function to be transformed, F(k_x, k_z) is the Fourier transform of the function and k_x and k_z are components of the wavenumber, k. Their relation given by the equation

$$k = \sqrt{k_x^2 + k_z^2}, \tag{2.18}$$

which relates to the wavelength λ in m by the equation

$$\lambda = \frac{2\pi}{k}. \tag{2.19}$$

As the relation between wavelength and velocity is known as

$$\lambda = \frac{c_s}{f_0}, \tag{2.20}$$

we get the following equation for shear wave speed

$$c_s = \frac{2\pi f_0}{k}. \tag{2.21}$$

The k-space transform has successfully been implemented as an image reconstruction mode for MRI data, and is regularly used for the reconstruction and analysis of MRI data [44]. It is also a central method in some ultrasound simulations [45].

Now lets illustrate how these equations can be used in vibration elastography. We assume that we vibrate tissue with a sinusoidal excitation of frequency f_0, so that shear waves are generated all over the domain. Let us assume that there are two regions in the domain, each with different elastic properties, so that shear waves travel at 10 m/s in a top layer and at 5 m/s in the bottom one.

From equation (2.20) and the fact that the temporal frequency f_0 is the same in both regions, we see that the top region will show a longer wavelength than the bottom one. Figure 2.5 illustrates this point. On the left-hand side we see a map of the velocity field for such scenario.

If we apply the Fourier transform to the velocity field we obtain a representation of the two different spatial frequencies as two distinctive peaks, shown on the right-hand side of Figure 2.5.

As k-space is periodic for real signal, copies of the two peaks are shown in k-space. The distance from the peak to the center of the spectrum (k=0) gives us the wavenumber associated with that field. These peaks are the major components of the k-space, and will from now on be referred to as components. Using equation (2.21) we can then estimate the shear wave velocity from the wavenumber.

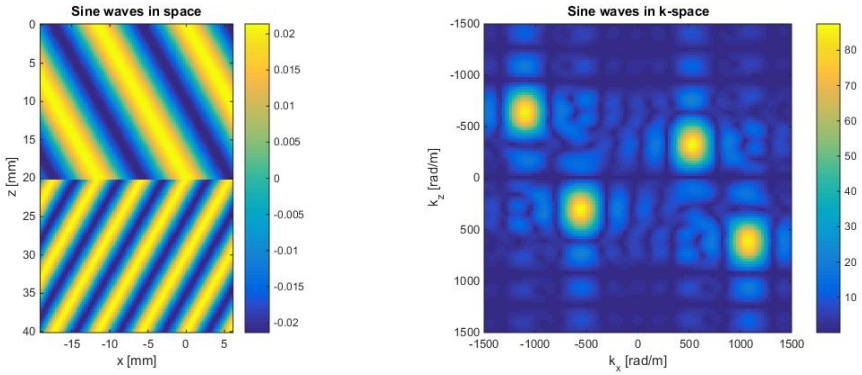

Figure 2.5: An example of how a set of waves looks like in space (left) and k-space (right)

2.3.4 Frequency Spectrum

The spectral energy density, or frequency spectrum, shows how the energy of the signal is distributed over different frequencies. The energy distribution S_{xx} of a signal $f(x)$ is given by

$$S_{xx}(f) = |\hat{x}(f)|^2 \tag{2.22}$$

with $\hat{x}(f)$ defined as the Fourier transform of the signal (see equation (2.13)). The method works with unidimensional frequency spectra, with respect to k. In order to convert the 2D frequency spectrum into a 1D signal, the relation (2.18) is used. The spectrum is then averaged over the interval $[0, \pi]$ making it independent of the direction of propagation. An example of a frequency spectrum is shown in Figure 2.6. We can clearly observe two components, or peaks, in the spectrum, one at about 5 and another at about 10 m/s.

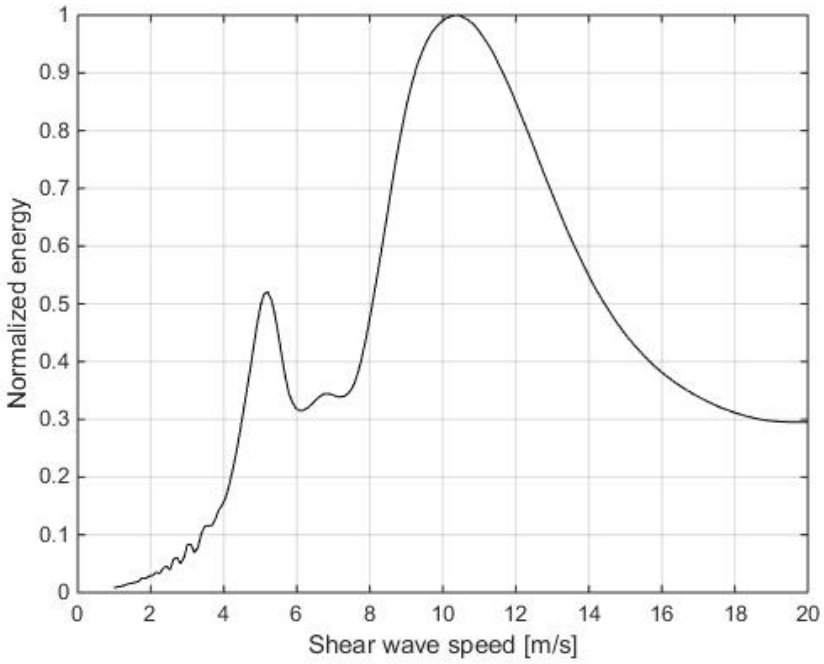

Figure 2.6: The frequency spectrum of the k-space of the two sine example in Figure 2.5

2.3.5 Filtering

When applying the k-space transform to a velocity field, a number of components may appear. Each distinct velocity in the velocity field will correspond to a component in k-space, with a different distance from the origin. As seen in Figures 2.5 and 2.6 different components has different wavenumbers. They might be separable by tailoring filters to the components wavenumber and bandwidth. To take all propagation directions into account, the filter should be ring shaped, covering all directions from 0 to 2π.

To generate the filters a feature extraction method called peak detection was used on the spectra of the k-space. The peak detection finds the peaks in the spectrum and sorts them by prominence, which is the height of the peak compared to its neighbourhood. The two most prominent peaks were assumed to correspond to the two most interesting areas in k-space. When calculating the filters, the wavenumber corresponding to each peak was used as a midpoint for the ring filter, and the width of the filter was set as the estimated width of the peak.

After filtering, the inverse k-space transformation given in equation (2.17) can be used to extract the spatial information associated to each component. Figure 2.7 shows the peaks detected by the feature extraction method, and Figure 2.8 shows the k-space after filtering on the two major components and the velocity space after filtering.

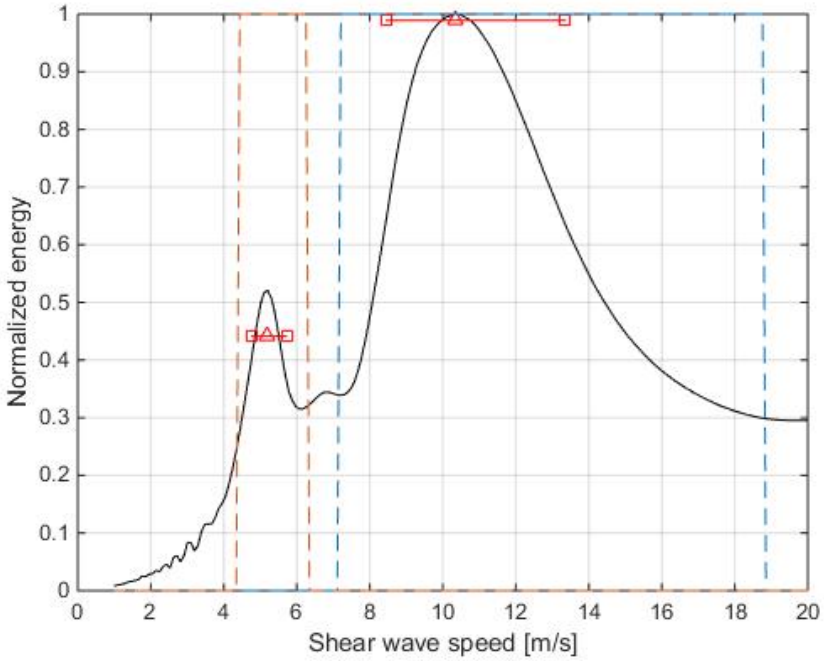

Figure 2.7: The detected peaks and resulting cutoff frequencies for the ring filters

2.3.6 Shear wave velocity field

While the velocity field shows the waves and their wavelengths, it does not automatically indicate which area has which wave speed. By adding up all the frames of a filtered velocity field, with absolute values, a cumulative velocity field was reached. It would indicate the area in which the filtered component existed, and was tagged by its wavenumber. The shear wave velocity field was estimated by calculating the sum of the two cumulative velocity fields, weighted by their wavenumbers converted to shear wave speed by equation (2.21). A shear wave velocity field is shown in Figure 2.9, and clearly indicates the wave speeds in both fields.

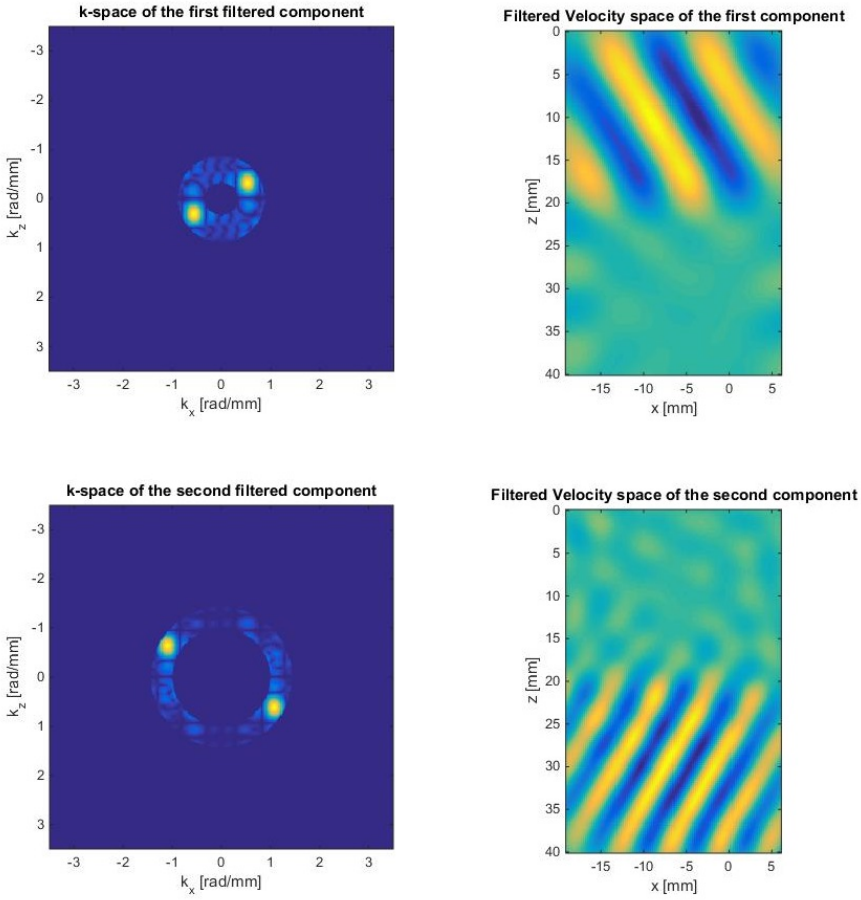

Figure 2.8: An example of a filtered k-space(left) and the resulting velocity field(right)

2.4 Phantoms

In ultrasound an imaging phantom, or just phantom, is an object used to test the performance of imaging equipment or methods. They are designed with specific physical properties, and may include inhomogeneities. They can be made in different ways, and from diverse materials, like silicone, gelatin, agar or polyvinyl alcohol (PVA). Imaging phantoms are widely used in research because they provide a ground truth. They also make it possible to test methods that have not been approved for clinical research.

PVA phantoms are widely used in sonoelastography research as their mechanical properties can be tailored through cryogenic procedures [46]. A PVA phantom is made by mixing PVA-powder, a scattering agent (if needed) and water. The solution is heated to 90°C and poured

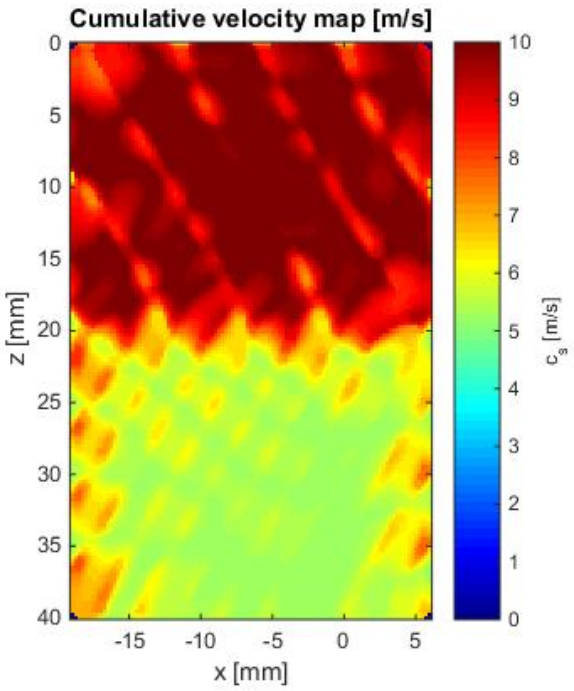

Figure 2.9: An example of a shear wave velocity map, calculated from the 2field case shown in Figure 2.5

into a mold. The mold is then ran through a number of Freeze-Thaw cycles (FT-cycles). A FT-cycle consists of a freeze and a thaw phase, usually of equal duration. This has been done successfully at several different lengths of both freeze time and thaw time, as well as with different temperatures [47] [46]. PVA phantoms can also be made in automatic temperature chambers. Each FT-cycle causes more "crosslinking of hydroxyl groups by hydrogen bonding" [47], and thus stiffens the phantom. The density of both PVA powder and scattering agent has also been shown to change the physical properties [46]. Figure 2.10, 2.11 and 2.12 shows the properties Jérémie Fromageau et al. found when testing different numbers of FT-cycles as well as different concentration of acoustic scatterer.

2.5 Hypothesis

Our hypothesis is that we can use k-space filtering techniques to create shear wave velocity maps in the following way: First, we expose the tissue under study to a stationary vibration field. Second, we estimate the spatial velocity field using Doppler techniques. Third, we express

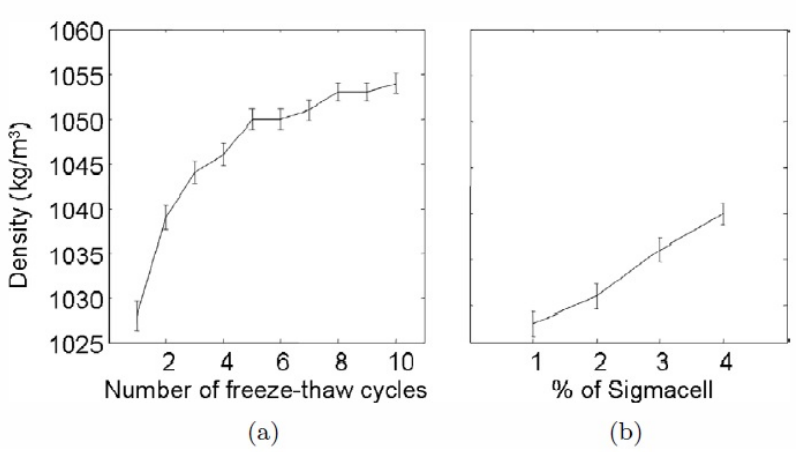

Figure 2.10: Density of PVA samples. (a) As a function of the number of freezing-thawing cycles for 3% Sigmacell. (b) As a function of the percentage of Sigmacell for two freezing-thawing cycles. Graph taken from Jérémie Fromageau et al. [46]

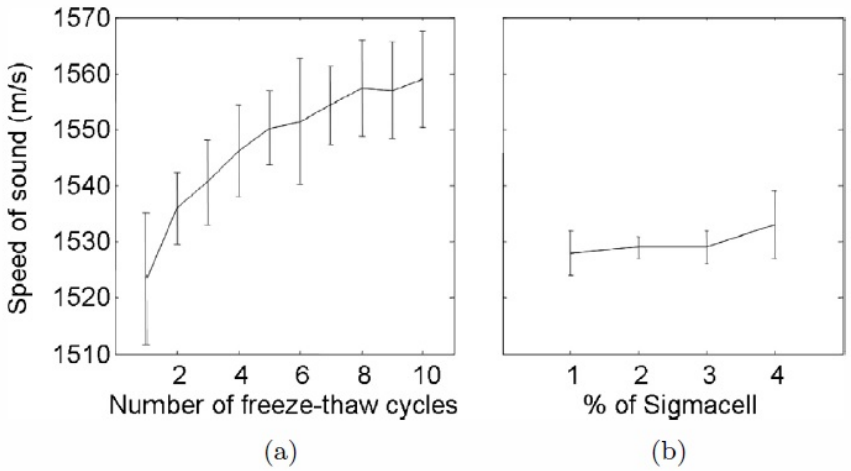

Figure 2.11: Speed of sound in PVA samples. (a) As a function of the number of freezing-thawing cycles for 3% Sigmacell. (b) As a function of the percentage of Sigmacell for two freezing-thawing cycles. Graph taken from Jérémie Fromageau et al. [46]

the spatial velocity field in k-space and we separate the different components using adaptive ring filters. Fourth, we extract the spatial information associated to each component using the inverse Fourier transform. And fifth, we generate a shear wave velocity map by combining the extracted spatial information and the detected velocities.

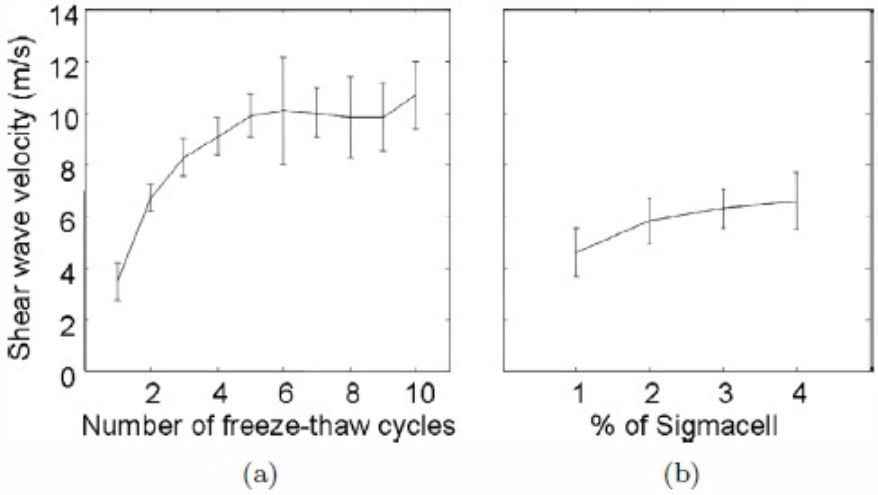

Figure 2.12: Shear wave speed in PVA samples. (a) As a function of the number of FT-cycles for 3% Sigmacell. (b) As a function of the percentage of Sigmacell for two FT-cycles. Graph taken from Jérémie Fromageau et al. [46]

Chapter 3

Materials and methods

The method described in Chapter 2 was tested on experimental and numerical data. In order to asses the methods ability to detect both softer and stiffer anomalies, two scenarios were considered in each dataset. The following section will describe the methods and materials used to acquire the data.

3.1 Numerical simulations

A 2D linear elastic model was solved with the finite element method (FEM) using Comsol Multiphysics 5.2 (Comsol, Burlington, USA). A domain was defined comprising a 15 mm radius cyst in a 40 x 40 mm region. Two sets of simulations were produced: one with a stiff cyst (shear wave speed 10 m/s) in a soft background (shear wave speed 5 m/s), and another with a soft cyst (5 m/s) in a stiff background (10 m/s). A harmonic excitation was used. An axial vibration source was set at the bottom boundary of the domain producing both pressure and shear waves of the desired frequency. The simulations were solved in the frequency domain for 500, 1000 and 2500 Hz. The 2D velocity fields (v_x, v_z) were obtained from the simulation result. The velocity in the axial direction v_z was taken as the tissue doppler velocity. Figure 3.1 shows and example of the axial velocity field for the two scenarios considered: stiff and soft cyst. Figure 3.2 shows the mesh used to perform the calculation at 500 Hz.

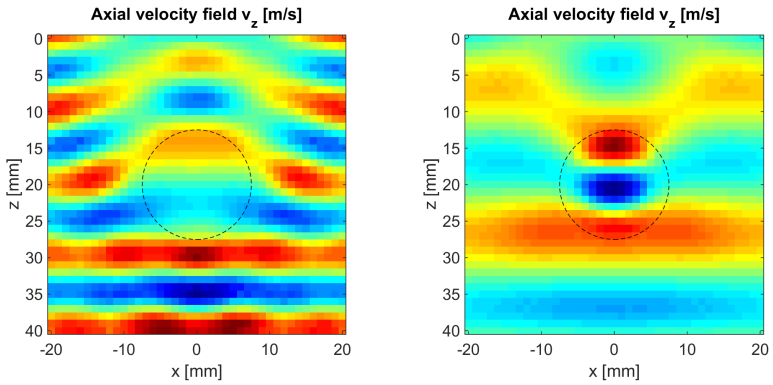

Figure 3.1: Axial velocity field v_z for the numerical data, hard (left) and soft (right) cyst scenarios at 500 Hz

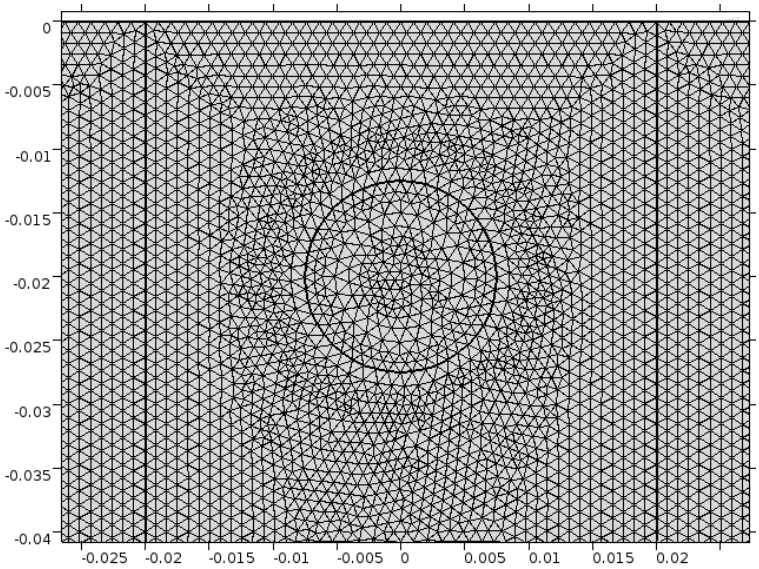

Figure 3.2: Spatial discretization used for the numerical simulation at 500 Hz.

3.2 Experimental methods

3.2.1 PVA phantom production

The PVA phantoms used for the experimental data were made using 10% PVA, 0.5% Orgasol (Polyamide powder) and 89.5% water, all by weight. In total 250 mL PVA solution was made, using 1.25 g Orgasol, 25 g PVA and 223.75 g water. The materials were mixed in a 500 mL Erlend Meyer flask and heated to 90°C while stirring with a magnetic stirrer, at a suitable speed to ensure thermal homogeneity while avoiding the generation of air bubbles. Once heated to 90°C, it was cooled in an ice bath with continued stirring down to room temperature. This liquid was

then poured into four 3D-printed molds: 2 rectangular prisms with a cylindrical protrusion in the center as shown in Figure 3.3, and two cylindrical molds corresponding to the protrusions as shown in Figure 3.4. The molds were designed so that the phantoms could be put together to two complete prisms, as shown in Figure 3.6. All four of the molds was ran through 3 Freeze-thaw cycles (FT-Cycles) of 12h at -20°C followed by 12h at room temperature, and then one of each got 2 more FT cycles to be the harder parts of the phantoms. Figure 3.5 shows how they looked after all FT-Cycles. Estimates of the properties of the phantom was made using Figures 2.10, 2.11 and 2.12, and are listed in Table 3.1.

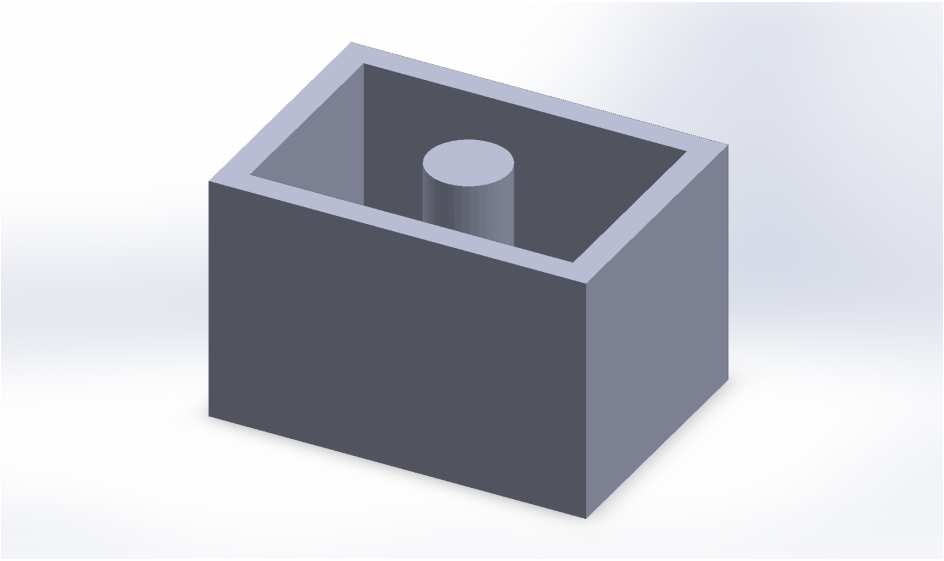

Figure 3.3: The shape of the mold used for the area outside of the cyst

	Density [kg/m^3]	Speed of Sound [m/s]	Shear wave speed [m/s]
Soft Phantom	1035	1540	6
Hard Phantom	1040	1550	10

Table 3.1: Estimated density and speed of sound for the PVA phantoms

3.2.2 Experimental apparatus

The PVA phantom was placed on a 10 mm aluminium slab rigidly connected to a 26 Watts vibration speaker (Mighty Dwarf, Milton, Ontario Canada). To reduce reverberation a 10 mm thick acoustic absorber (AptFlex F28, Precision Acoustics, Dorchester, UK) was placed between the aluminium slab and the test sample. Both the acoustic absorber and the test sample were fixed

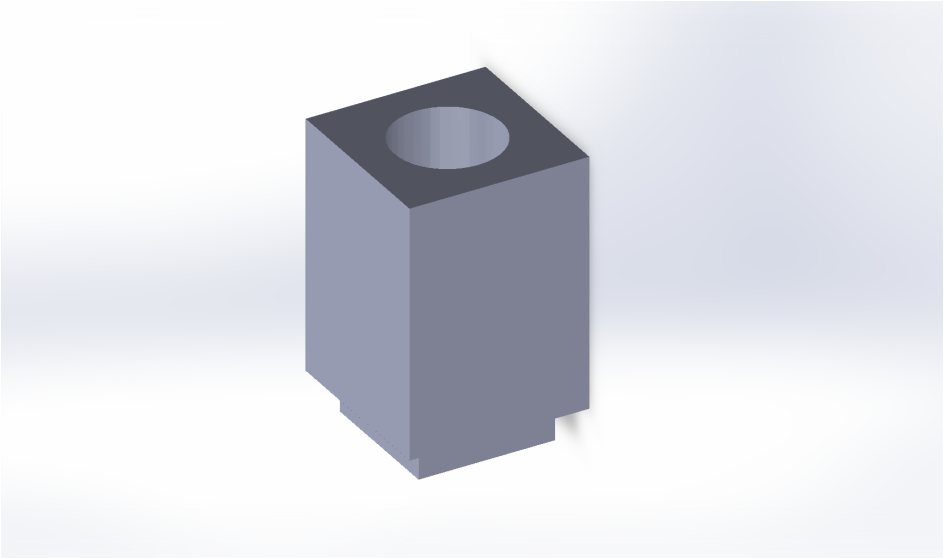

Figure 3.4: The shape of the mold used for the cyst

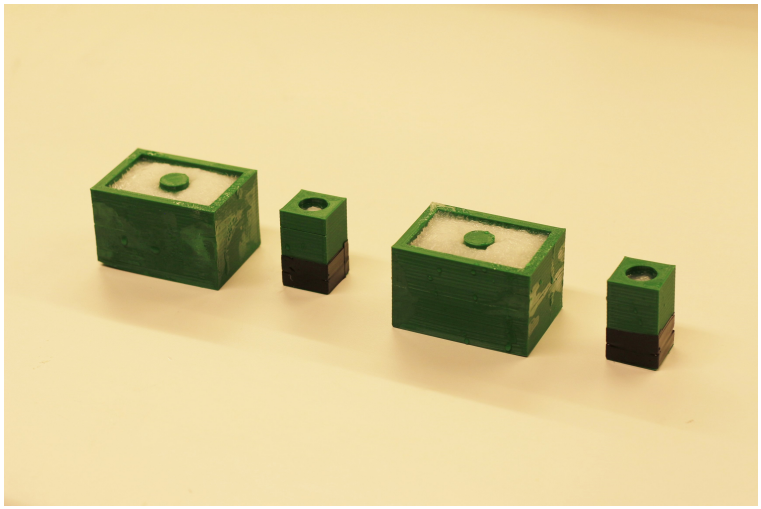

Figure 3.5: The PVA phantoms in their molds

with double-sided tape to the aluminium slab to prevent sliding. A sine wave was generated with a WW2571 Arbitrary Waveform Generator (Tabor Electronics, Nesher, Israel) and amplified with an Azur640A audio amplifier (Cambridge Audio, London, UK). The signal delivered to the speaker was monitored with a GDS-2062 Oscilloscope (GWINSTEK, New Taipei City, Taiwan). The generated vibration was in the axial direction. However, due to the impossibility of a perfect alignment, shear waves were produced traveling in different directions.

A Verasonics Vantage 256 research scanner and a L11-4v 300 μm probe were used to estimate

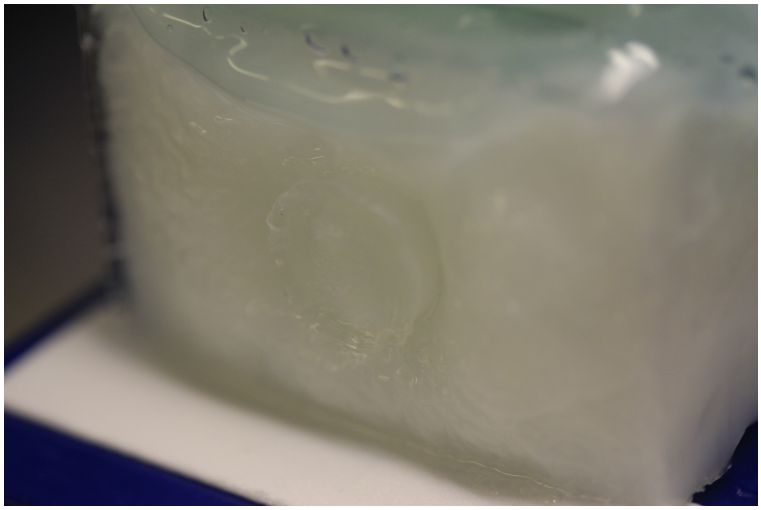

Figure 3.6: Closeup of the phantom, showing the cyst

the velocity field in the test subject. A plane-wave imaging sequence was used with a PRF of 3450 Hz. The transmit frequency was 5.2 MHz. Channel data was recorded using MATLAB and beamformed using the USTB. The axial velocity field was then estimated using equation (2.12). Figure 3.7 shows the experimental setup.

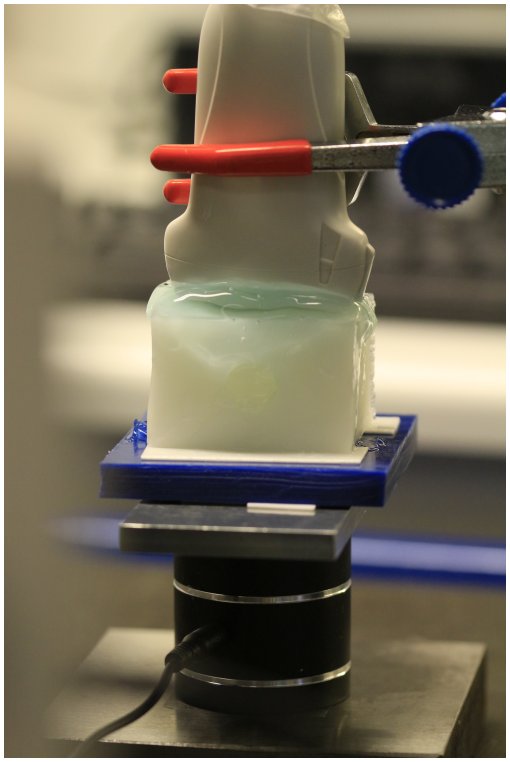

Figure 3.7: The experiment setup

Chapter 4

Results

According to the methods specified in Chapter 2, this Chapter will present numerical and experimental data to check the hypothesis stated in Section 2.5.

4.1 Numerical results

In the following two Subsections results are presented for the hard and soft cyst scenarios of numerical data. For each scenario the frequencies 500, 1000 and 2500 Hz have been tested. The expected velocities for the hard and soft cyst scenarios are shown in Table 4.1.

Cyst	c_s inside [m/s]	c_s outside [m/s]
Hard	10	5
Soft	5	10

Table 4.1: Values used in the numerical simulations for the velocities inside and outside of the cyst

4.1.1 Hard cyst

Figure 4.1 shows the axial velocity field calculated numerically for the hard cyst scenario using the excitation frequencies 500, 1000 and 2500 Hz. As expected it is observed that the wavelength inside the cyst is larger than outside the side. Figure 4.2 shows the the k-space transform of the axial velocity fields in Figure 4.1. The wavenumbers associated to the expected shear wave ve-

locities (5 and 10 m/s) are also displayed as circles in k-space. For the high frequency scenarios (1000 and 2500 Hz) we can see that energy concentrates at the expected wavenumbers.

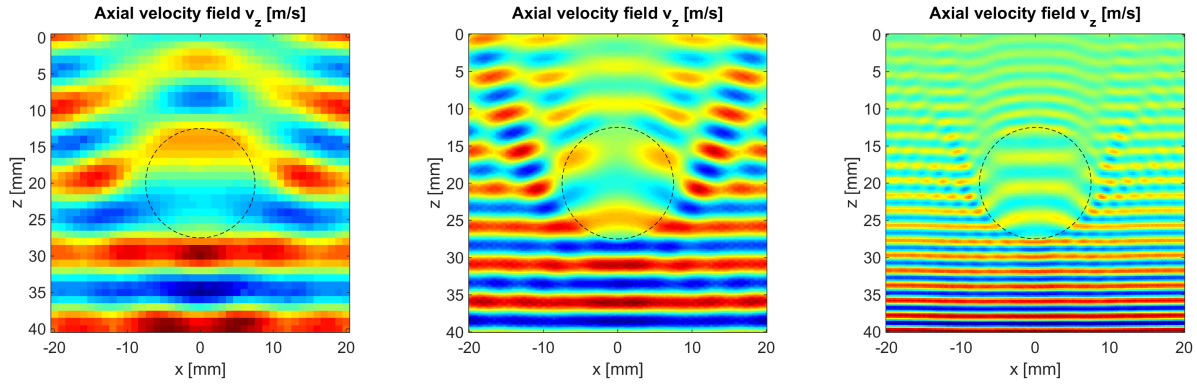

Figure 4.1: Axial velocity field v_z for the numerical data, hard cyst scenario at 500 Hz (left), 1000 Hz (middle) and 2500 Hz (right).

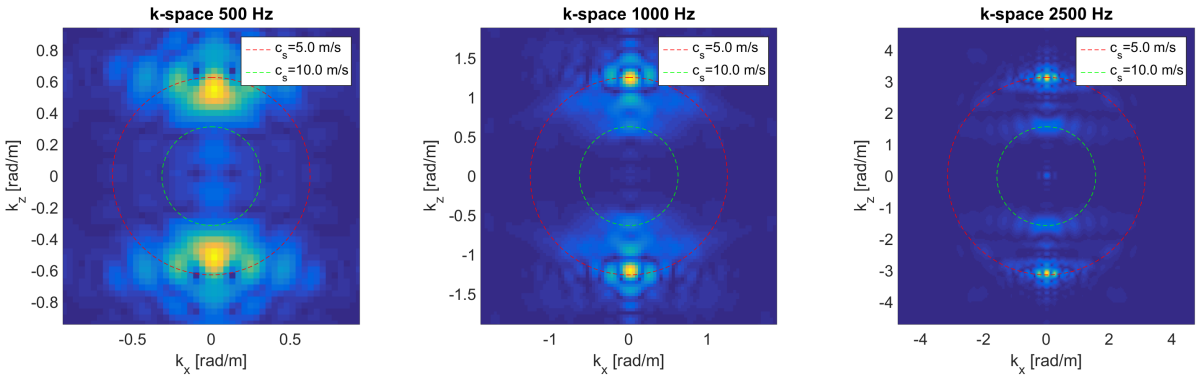

Figure 4.2: k-space for the numerical data, hard cyst scenario at 500 Hz (left), 1000 Hz (middle) and 2500 Hz (right).

Figure 4.3 shows the shear wave velocity maps for the numerical hard cyst scenario using the excitation frequencies 500, 1000 and 2500 Hz. We observe that the delineation of the cyst improves with frequency. Table 4.2 shows the mean value and standard deviations of the shear wave speed inside and outside the cyst. In effect we observe that the numerical values get closer to the expected values (10 and 5 m/s) as the frequency increases.

Frequency [Hz]	c_s inside [m/s]	c_s outside [m/s]
500	5.86 ± 0.04	5.61 ± 0.55
1000	7.84 ± 0.55	5.75 ± 0.46
2500	9.19 ± 0.13	5.30 ± 0.33

Table 4.2: The mean wave speeds inside and outside of the cyst in the maps of the hard, numerical data in Figure 4.3 with one standard deviation

Using a 500 Hz excitation the estimated shear wave velocities inside and outside the cyst become almost identical (5.9 - 5.6 m/s) and the cyst goes undetected. Using a 1000 Hz excitation the cyst is detected in its true location. Its estimated size and shape, however, is inaccurate. The estimated shear wave velocities inside and outside become more precise (7.8 - 5.8 m/s). With a 2500 Hz excitation the cyst is rendered with precision. The estimated shear wave velocities (9.2 - 5.3 m/s) become very close to the ground truth.

Figure 4.4 shows the velocity field of the two first detected components when a 2500 Hz vibration signal is used. The first component (5.1m/s) corresponds to the expected shear wave velocity outside the cyst, and accurately demarcate the area outside of the cyst. The second component (9.8m/s) is very close the expected value, and delineates with precision the area inside the cyst.

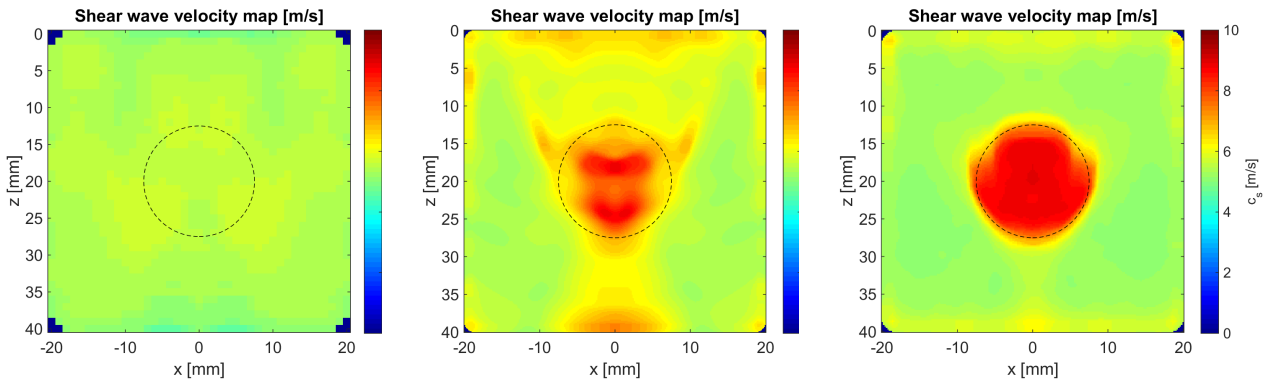

Figure 4.3: Shear wave velocity map for the numerical data, hard cyst scenario at 500 Hz (left), 1000 Hz (middle) and 2500 Hz (right).

The plots in Figure 4.5 show the the spectra of the whole domain, inside the cyst, and outside the cyst. It compares the spectra for the vibration frequencies 500 and 2500 Hz. While the two spectral component are easily identified in the 2500 Hz spectra, they become merged at 500 Hz.

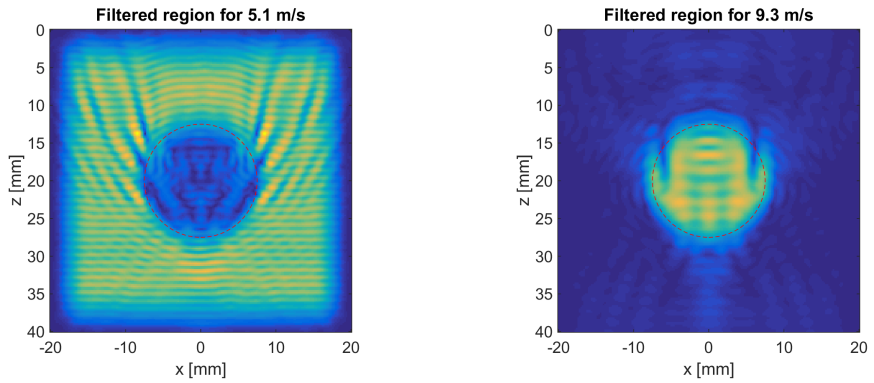

Figure 4.4: The velocity fields corresponding to the first (left) and second (right) detected components for the numerical, hard cyst excited by a 2500 Hz signal

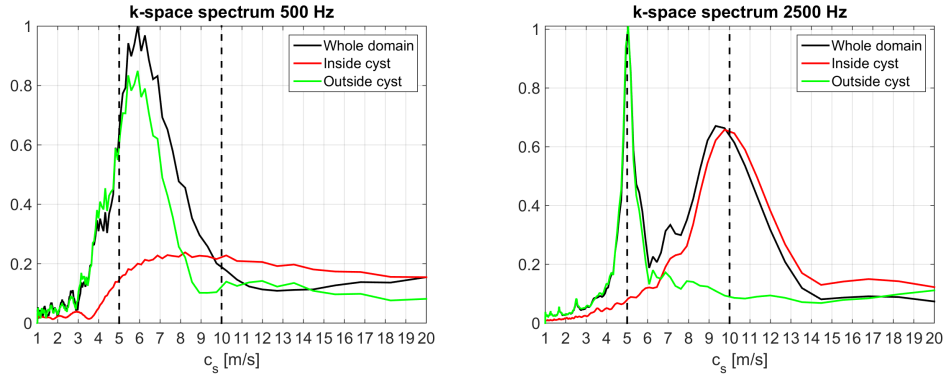

Figure 4.5: The frequency spectra of the numerical, hard cyst excited at 500 (left) and 2500 Hz (right)

4.1.2 Soft cyst

Figure 4.6 shows the axial velocity field calculated numerically for the soft cyst scenario using the excitation frequencies 500, 1000 and 2500 Hz. As expected it is observed that the wavelength outside the cyst is larger than inside the side. Figure 4.7 shows the the k-space transform of the axial velocity fields in Figure 4.6. The wavenumbers associated to the expected shear wave velocities (5 and 10 m/s) are also displayed as circles in k-space. As in the previous case, we observe that energy concentrates at the expected wavenumbers for the high frequency scenarios (1000 and 2500 Hz).

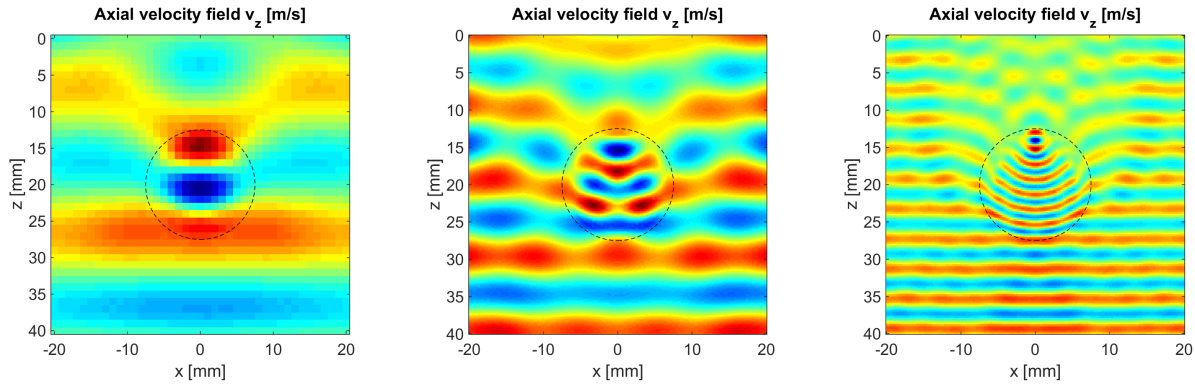

Figure 4.6: Axial velocity field v_z for the numerical data, soft cyst scenario at 500 Hz (left), 1000 Hz (middle) and 2500 Hz (right).

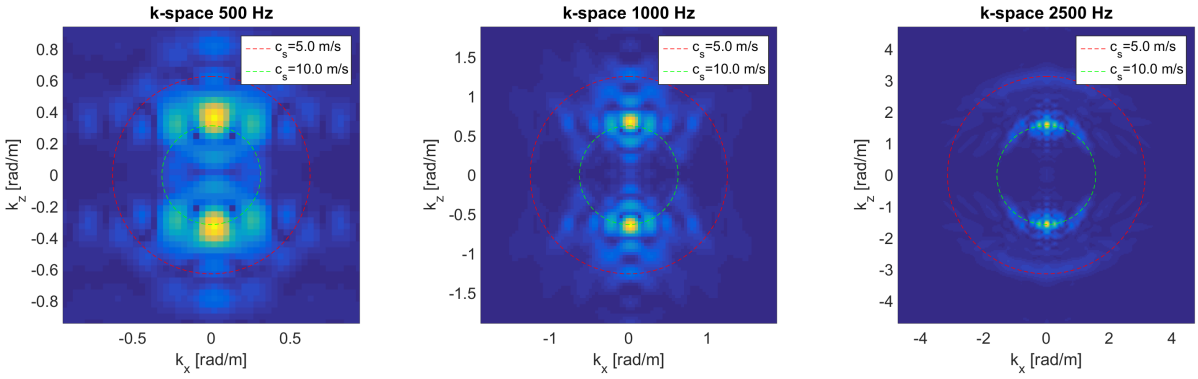

Figure 4.7: k-space for the numerical data, soft cyst scenario at 500 Hz (left), 1000 Hz (middle) and 2500 Hz (right).

Figure 4.8 shows the shear wave velocity maps for the numerical soft cyst scenario using the excitation frequencies 500, 1000 and 2500 Hz. We observe that the delineation of the cyst improves with frequency. Table 4.3 shows the mean value and standard deviations of the shear wave speed inside and outside the cyst. In effect we observe that the numerical values get closer to the expected values (5 and 10 m/s) as the frequency increases.

Frequency [Hz]	c_s inside [m/s]	c_s outside [m/s]
500	7.11 ± 0.19	7.11 ± 0.77
1000	5.99 ± 0.31	7.91 ± 0.57
2500	5.77 ± 0.20	9.26 ± 0.65

Table 4.3: The mean wave speeds inside and outside of the cyst in the maps of the soft, numerical data in Figure 4.8 with one standard deviation

Using a 500 Hz excitation the estimated shear wave velocities inside and outside the cyst be-

come identical (7.1 m/s) and the method fails to detect the cyst. The cyst is detected in its true location if a 1000 Hz vibration is used. However the estimation of its shape and size is imprecise. The estimated shear wave velocities get closer to the ground truth (6.0 - 7.9 m/s). The estimated shear wave velocities become very accurate (5.8 - 9.3 m/s) when a 2500 Hz vibration is used. The cyst shape and location is displayed correctly.

Figure 4.9 shows the velocity field of the two first detected components when a 2500 Hz vibration signal is used. The first component (9.8 m/s) corresponds to the expected shear wave velocity outside the cyst, and accurately demarcate the area outside of the cyst. The second component (5.1 m/s) is very close the expected value, and delineates with precision the area inside the cyst.

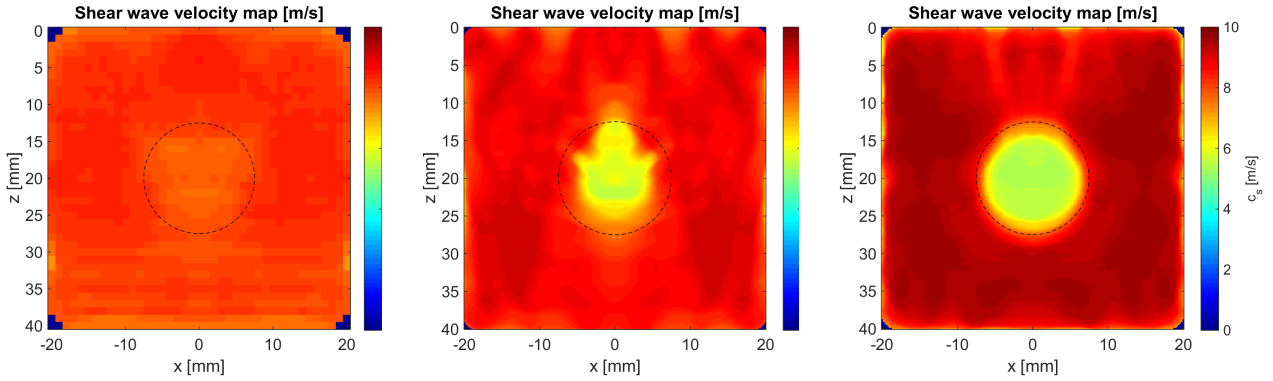

Figure 4.8: Shear wave velocity map for the numerical data, soft cyst scenario at 500 Hz (left), 1000 Hz (middle) and 2500 Hz (right).

The plots in Figure 4.10 show the spectrum of the whole domain, the spectrum of inside the cyst, and spectrum of outside the cyst. It shows the spectra for the vibration frequencies 500 and 2500 Hz. While the two spectral component are easily identified in the 2500 Hz spectrum, the 500 Hz spectrum is a bit more complex. There is a large peak at 8 m/s, which is a bit lower than the expected 10 m/s. We also see a peak at 4 m/s, a bit lower than the expected 5 m/s, as well as a smaller peak around 5.5 m/s, a bit higher than the expected 5 m/s.

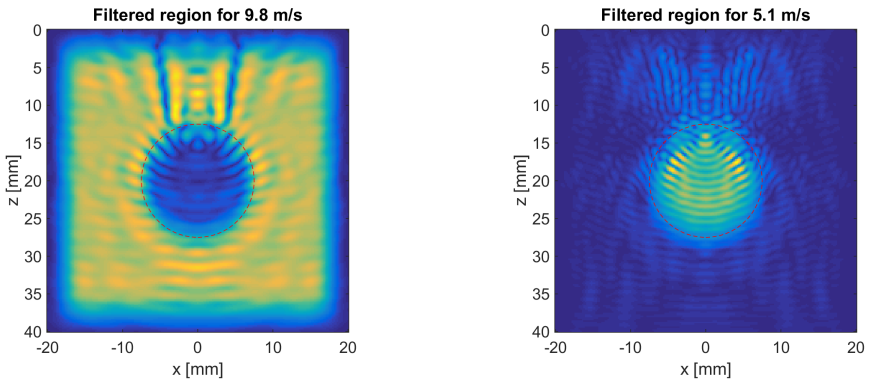

Figure 4.9: The velocity fields corresponding to the first (left) and second (right) detected components for the numerical, soft cyst excited by a 2500 Hz signal

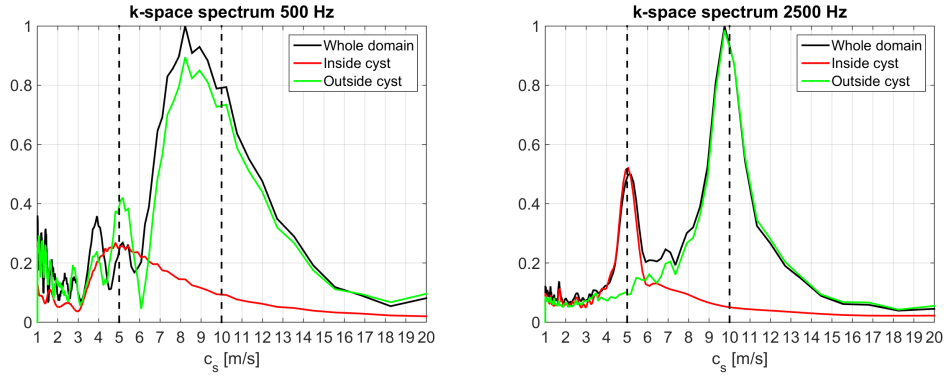

Figure 4.10: The frequency spectra of the numerical, soft cyst excited at 500 (left) and 2500 Hz (right)

4.2 Experimental Results

In the following two Subsections results are presented for the hard and soft cyst scenarios of experimental data. For each scenario the frequencies 300, 500 and 1000 Hz have been tested. The expected values for the soft and hard cyst scenarios are shown in Table 3.1. It was noted during the experiment that at higher frequencies, around 1000 Hz and upwards, the phantom would barely show any vibration, even at maximum amplitude.

4.2.1 Hard cyst

Figure 4.11 shows the axial velocity field measured experimentally for the hard cyst scenario using the excitation frequencies 300, 500 and 1000 Hz. Only the velocity field at 300 Hz shows obvious wave structure, while at 500 and 1000 Hz the waves are too cluttered. Figure 4.12 shows

the k-space transform of the axial velocity fields in Figure 4.11.

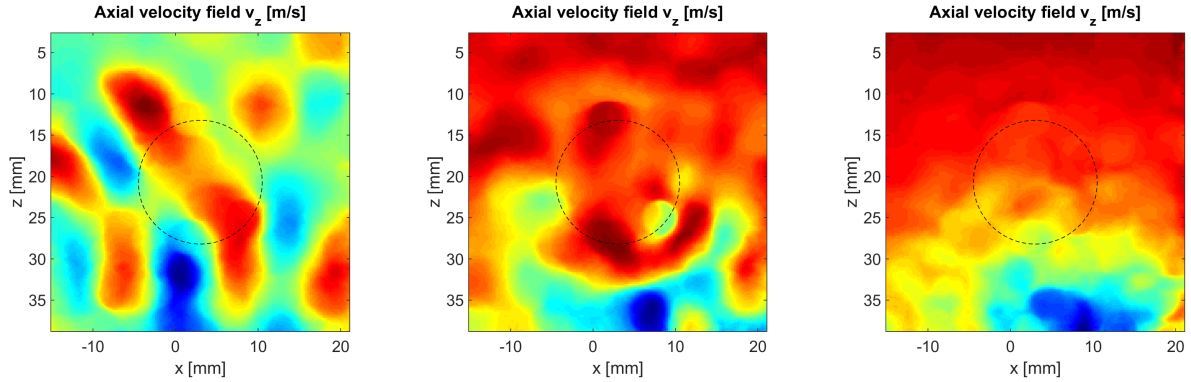

Figure 4.11: Axial velocity field v_z for the experimental data, hard cyst scenario at 300 Hz (left), 500 Hz (middle) and 1000 Hz (right).

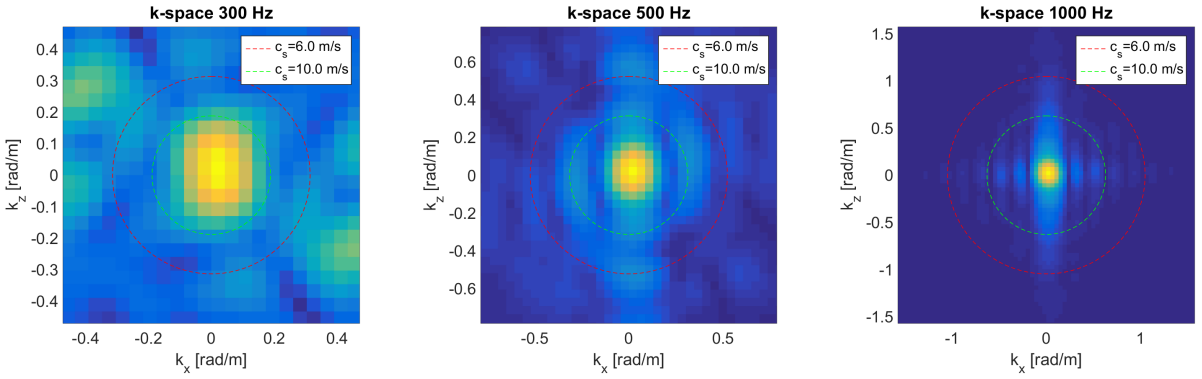

Figure 4.12: k-space for the experimental data, hard cyst scenario at 300 Hz (left), 500 Hz (middle) and 1000 Hz (right).

Figure 4.13 shows the shear wave velocity maps for the experimental hard cyst scenario using the excitation frequencies 300, 500 and 1000 Hz. We observe that the cyst is not correctly displayed for any of the frequencies used. Table 4.4 shows the mean value and standard deviations of the shear wave speed inside and outside the cyst. While the mean values for 300 Hz are very close to the expected values we can argue this is a mere coincidence. The standard deviation values are very high for the three cases.

Frequency [Hz]	c_s inside [m/s]	c_s outside [m/s]
300	8.50 ± 1.31	6.73±1.68
500	8.26±0.83	8.33±0.87
1000	6.15±0.37	6.15±0.36

Table 4.4: The mean wave speeds inside and outside of the cyst in the maps of the hard, experimental data in Figure 4.13 with one standard deviation

Using an excitation higher than 500 Hz the estimated shear wave velocities inside and outside the cyst become almost identical, and the cyst goes undetected. While something can be observed in the area where the cyst should be expected, we can argue it is a mere coincidence.

Figure 4.14 shows the velocity field of the two first detected components when a 300 Hz vibration signal is used. The first component (3.6 m/s) does not correspond to any of the expected shear wave velocities, but may correlate with the area outside of the cyst. The second component (13.8 m/s) does not correspond to any of the expected shear wave velocities, and does not correlate with any specific area.

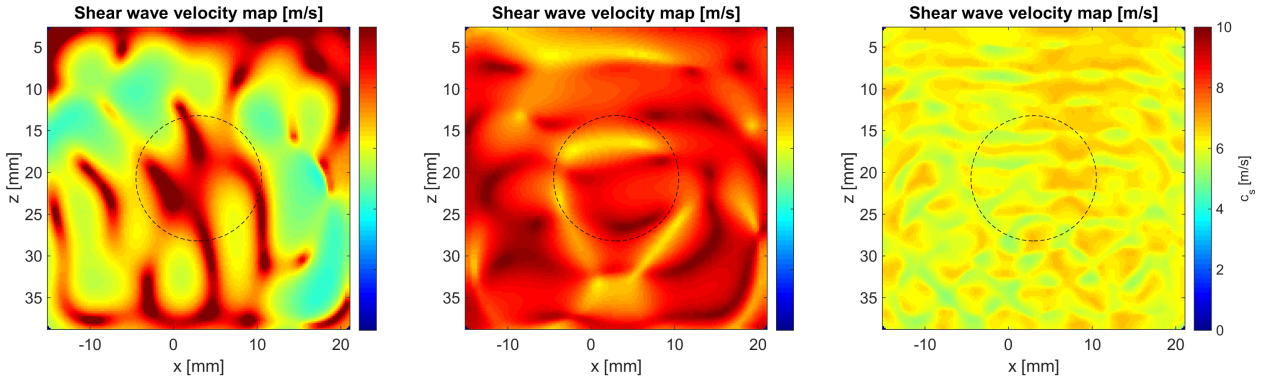

Figure 4.13: Shear wave velocity map for the experimental data, hard cyst scenario at 300 Hz (left), 500 Hz (middle) and 1000 Hz (right).

The plots in Figure 4.15 shows the spectrum of three signals: the signal in the whole domain, the signal inside the cyst, and the signal outside it. It compares the spectra for the vibration frequencies 300 and 1000 Hz. While two spectral components are easily identified in the 300 Hz spectra, neither of the peaks correspond to the expected values; there is one peak around 4 m/s and one around 14 m/s. At the higher frequency there are no distinct peaks indicated, only a steady incline towards higher velocities.

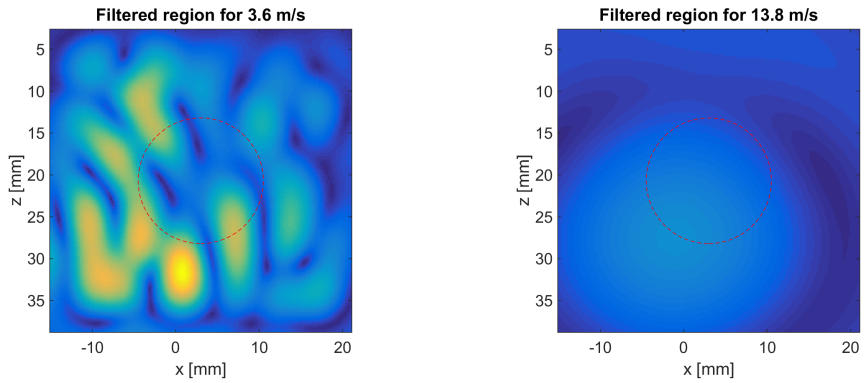

Figure 4.14: The velocity fields corresponding to the first (left) and second (right) detected components for experimental data of the soft cyst scenario excited by a 300 Hz vibration.

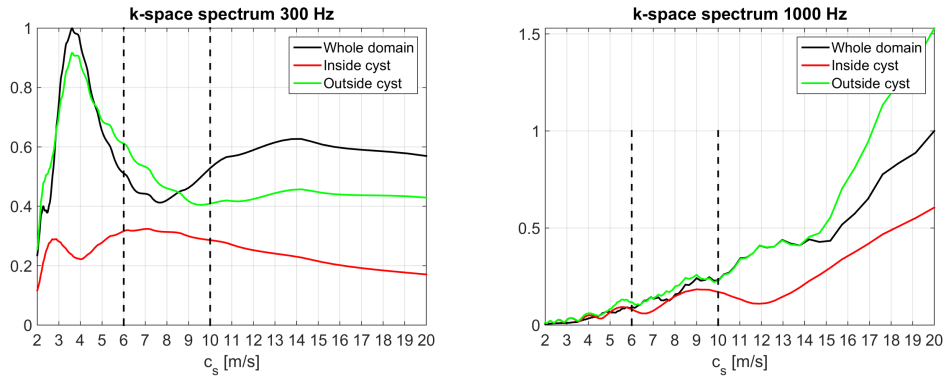

Figure 4.15: The frequency spectra of the experimental data for the hard cyst scenario excited by 300 (left) and 1000 Hz (right) vibration.

4.2.2 Soft cyst

Figure 4.16 shows the axial velocity field measured experimentally for the soft cyst scenario using the excitation frequencies 300, 500 and 1000 Hz. While some wavelike structure shows at both 300 and 500 Hz, all three frequencies are too cluttered. Figure 4.17 shows the the k-space transform of the axial velocity fields in Figure 4.16. The wavenumbers associated to the expected shear wave velocities (6 and 10 m/s) are displayed as circles in k-space. We observe that most energy is concentrated on the center of the k-space which corresponds to very low wavenumbers (i.e. very fast shear wave velocities). We observe some energy around the expected values (6 and 10 m/s) for the 300 and 500 Hz cases.

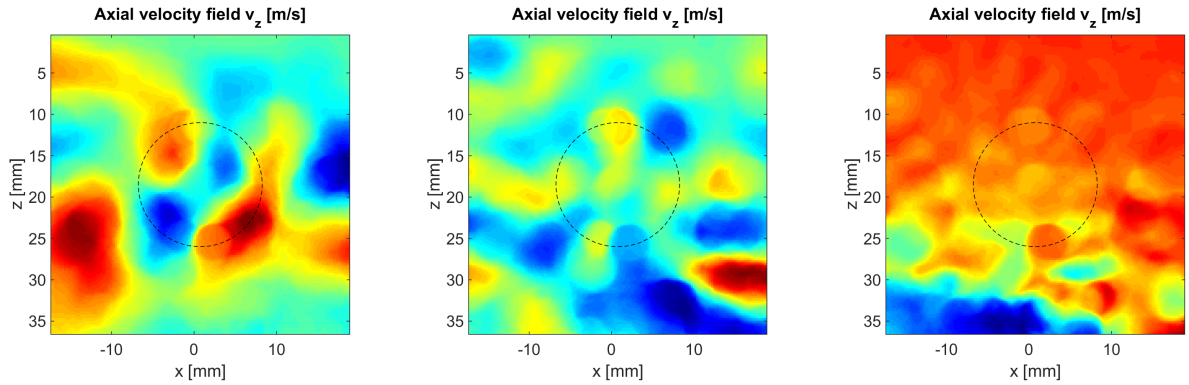

Figure 4.16: Axial velocity field v_z for the experimental data, soft cyst scenario at 300 Hz (left), 500 Hz (middle) and 1000 Hz (right).

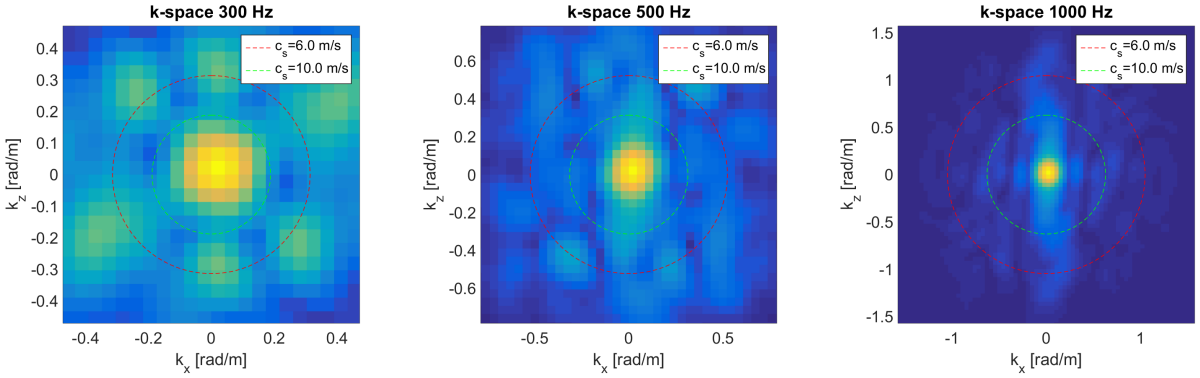

Figure 4.17: k-space for the experimental data, soft cyst scenario at 300 Hz (left), 500 Hz (middle) and 1000 Hz (right).

Figure 4.18 shows the shear wave velocity maps for the experimental soft cyst scenario using the excitation frequencies 300, 500 and 1000 Hz. The method fails to display the cyst in the expected region. Table 4.5 shows the mean value and standard deviations of the shear wave speed inside and outside the cyst. The estimated shear wave speeds are almost identical at all frequencies. At 300 Hz they are close to the expected value for the cyst, while at 1000 Hz they are close to the expected value outside the cyst.

Frequency [Hz]	c_s inside [m/s]	c_s outside [m/s]
300	6.24±1.01	6.49±1.31
500	4.88±0.20	4.96±0.25
1000	7.96±0.60	7.95±0.56

Table 4.5: The mean wave speeds inside and outside of the cyst in the maps of the soft, experimental data in Figure 4.18 with one standard deviation

Figure 4.14 shows the velocity field of the two first detected components when a 300 Hz vibration signal is used. The first component (4.7 m/s) does not correspond to any of the expected shear wave velocities, but may indicate the area inside the cyst. The second component (14.2 m/s) does not correspond to any of the expected shear wave velocities, and it does not correlate with any specific area.

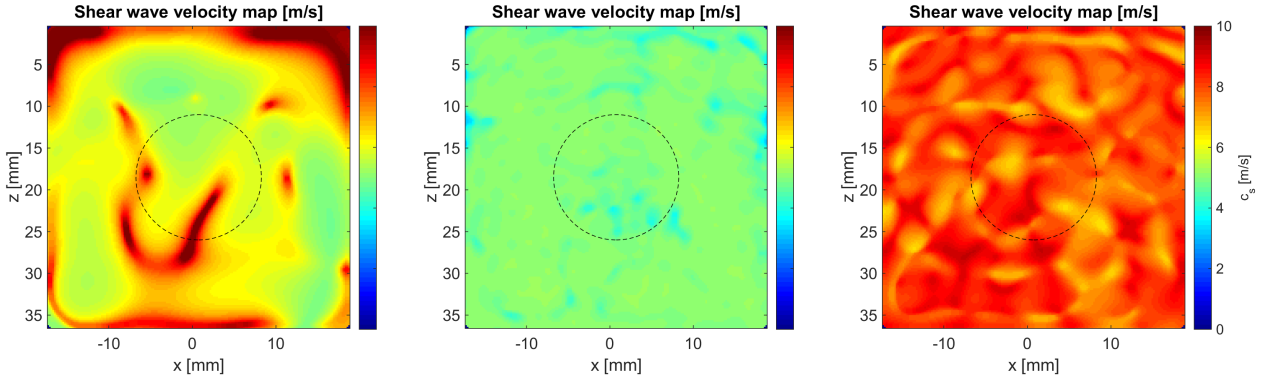

Figure 4.18: Shear wave velocity map for the experimental data, soft cyst scenario at 300 Hz (left), 500 Hz (middle) and 1000 Hz (right).

the spectra of the whole domain, inside the cyst, and outside the cyst The plots in Figure 4.20 shows the spectra of the inside of the cyst, the outside of the cyst and the whole domain. It compares the spectra for the vibration frequencies 300 and 1000 Hz. While two spectral components are easily identified in the 300 Hz spectra, neither of the peaks correspond to the expected values; there is one peak around 5 m/s and one around 14 m/s. At the higher frequency, there are also two distinguishable spectral components, the lower corresponding to the velocity inside the cyst, and the other a bit higher than the expected velocity outside of the cyst.

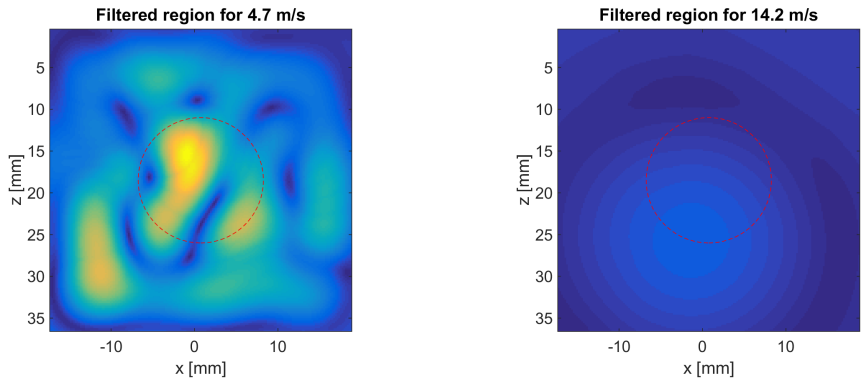

Figure 4.19: The velocity fields corresponding to the first (left) and second (right) detected components for experimental data of the soft cyst scenario excited by a 300 Hz vibration.

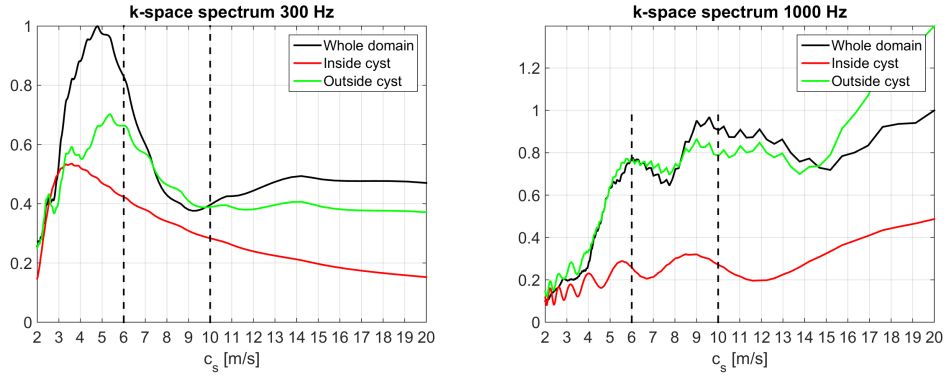

Figure 4.20: The frequency spectra of the experimental data for the soft cyst scenario excited by 300 (left) and 1000 Hz (right) vibration.

Chapter 5

Discussion

The following section will discuss the results presented in Chapter 4, their implications for the method as well as analyzing some of its limitations and how to possibly address them.

As shown in equation (2.21), the wave speed in space is inversely proportional to the wavenumber k, and proportional to the frequency. In addition, as real waves have a bandwidth - they are not just one frequency, but consists of a band of frequencies, they will also have some spread in k-space. As c_s has to remain constant for a given region, increasing f_0 will increase the distance between any two points in k-space. For example, by doubling the value of f_0, we also double the distance between the wavenumbers of $c_s = 10$ m/s and $c_s = 5$ m/s. As the bandwidth of the peaks do not increase at the same rate, judging from the results presented in Chapter 4, the peaks become orthogonal in k-space and hence easily separable.

This is illustrated in Figure 4.5, which shows the spectrum of the hard, numerical cases for frequencies 500 and 2500 Hz. We can see that the peaks overlap at 500 Hz, which hinders the methods ability to detect and discriminate between them. This also explains why the method was unable to detect the cyst in the experimental data, as the peaks in their spectra entirely overlap. When the frequency is increased, we observe that at $f_0 \approx 2500$ Hz, the method not only correctly estimates the shape and location of the cyst, but also provides an accurate estimation of the shear wave velocity values. As the peaks in the spectra are distinct, they are easily detected on the spectrum and isolated by the ring filter approach. One can hypothesize that better per-

formance could be obtained at even higher frequencies. In addition, spatial resolution increases at higher frequencies, providing a better delineation of the cyst.

The aim of this project was to investigate the feasibility of a k-space filtration technique to vibration sonoelastography and assessing its accuracy, validity and clinical feasibility. We can see from the numerical analysis that in some cases the method finds both the correct shear wave speed inside the cyst as well as its shape. The shear wave velocity map can be transformed into a shear modulus map by equation (2.5). This means the method can be used to process ultrasound data and map the hardness of eventual cysts in the inspected region, meaning it is both accurate and valid for clinical use. Compared to the vibro-acoustography and elastography using ARFI, the proposed approach has the advantage of being faster, as the filters can be calculated from just one frame, as well as having better penetration due to using an external source for the excitation, which is only limited by the power of the mechanical shaker.

That said, the method has limitations. Both the feature extraction and the ring filtering do not discriminate the propagation direction. However, in most cases the shear wave velocity fields show a mean propagation direction in the whole domain. Consequently some components that are easily separable in the k-space due to their distinct propagation directions become indistinguishable in the spectrum, or buried by the noise present at other propagation directions. This could be addressed by designing a detection and filtering strategy that takes into account the direction of propagation in k-space.

Alternatively, this could be addressed by modifying the measurement setup. By including a collection of vibration sources that excite the medium from different angles, the vibration field could be made more diffuse and hence less direction dependent. Having waves traveling in all directions would cause the k-space to have rings instead of just blobs. This would also increase the amount of information in the filtered area, and thus reduce signal to noise ratio of the filter.

Another limitation of the proposed method is that it tries to model a 3D space using 2D slices of it. For example, if you were to slice a cylinder normally to its height, you would get a circle of

the same radius as the cylinder, while if you cut it at an oblique angle, the resulting shape would be an ellipse with the long axis larger than the cylinder radius. Similarly, if the 2D slices of the 3D velocity field are not in the same direction as the propagation direction of the waves, called transverse waves, we will observe an unrealistic long wavelength and thus find unrealistically fast shear waves. This explains the blobs observed at very low wavenumbers in the experimental data (Figures 4.15 and 4.20) that were not present in the numerical results, and also explains why the method was unable to detect the cyst at 300 Hz despite there being two distinct peaks in the spectra (as seen in Figures 4.15 and 4.20). This problem could be addressed by performing 3D acquisition; sweeping the linear probe along the Y axis while scanning, which produces an estimation of the 3D shear wave velocity field.

While promising results were obtained in the numerical data, the proposed method did not work as well for the experimental data. The high attenuation of shear waves in the phantom prevented increasing the frequency above 1 kHz. However, a more powerful vibration source could make it possible to reach the good performance observed at 2500 Hz, especially if a 3D volume acquisition is performed.

Chapter 6

Conclusions

The aim of this project was to investigate the feasibility of a k-space filtration technique to produce elasticity maps with stationary vibration fields. To assess feasibility, numerical and experimental experiments were conducted. Elastography phantoms were produced and tested with an ultrasound research scanner. The method was implemented in a MATLAB routine and tested against the two sources of data.

We have seen that using vibration frequencies below 1000 Hz the method is unable to correctly detect the cyst in both experimental and numerical data, as the peaks in the spectrum overlap. In numerical data at 2500 Hz the method successfully extracts both the speed and the shape of the cyst. This shows that the k-space filtering approach can be viable for sonoelastography data at high frequencies, despite only showing it for numerical data in this experiment. The method did not perform well against experimental data due to limitations in the maximum achievable vibration frequency and due to the interference of vibration modes transversal to the imaging plane. Results indicate that, although it may be possible to use a k-filtering approach to improve the detection of breast cancer, further work is needed to increase the vibration frequency and to include the velocity estimation in 3D. By doing so it may be possible to increase the reliability and sensitivity of breast cancer screening.

For another attempt at this experiment, a a more powerful vibration source would be imperative, to ensure the vibrations reach throughout the phantom at high frequency. At higher

amplitude, I would also recommend having an automatic system for activation and deactivation of the vibrations, ensuring the source is only on for the barest minimum of time, as the noise could be a source of discomfort for both patient and operator.

Expanding the system with more sources of vibration around the inspected region could make the vibration field more diffuse and less direction dependent, which could improve the system.

In a prospective clinical use, a classification scheme could also be implemented: automatically deciding whether or not there are stiff anomalities in the inspected region.

Finally, changing the acquisition scheme from a 2D to a 3D acquisition scheme seems to be a compelling need of the method to deal with transversal vibration modes. Doing a 3D simulation study to get better correspondence to the experimental observations is advisable.

Bibliography

[1] The Norwegian institute for population-based cancer research. Statistics on breast cancer. http://www.kreftregisteret.no/no/Generelt/Fakta-om-kreft-test/Brystkreft-Alt2/, 2016. Accessed: 2016-04-26.

[2] MacMahon B. Epidemiology and the causes of breast cancer. *Int. J. cancer*, 118:2373–2378, 2006.

[3] The Norwegian institute for population-based cancer research. The mammography-project. http://www.kreftregisteret.no/no/Forebyggende/Mammografiprogrammet/Organisering/, 2016. Accessed: 2016-04-26.

[4] Huangdi neijing. https://en.wikipedia.org/wiki/Huangdi_Neijing, 2016. Accessed: 2016-05-15.

[5] Breasted J. H. The edwin smith surgical papyrus: published in facsimile and hieroglyphic transliteration with translation and commentary in two volumes. *Chicago: University of Chicago Press*, 1991.

[6] The free dictionary. http://medical-dictionary.thefreedictionary.com/palpation, 2016. Accessed: 2016-04-28.

[7] Szabo T.L. *Diagnostic Ultrasound Imaging, Inside Out.* Academic Press, 2004, 1 edition, 2004.

[8] Singh S. and Goyal A. The origin of echocardiography: A tribute to inge edler. *Texas Heart Institute Journal.*, 34:431–438, 2007.

[9] Otto C.M. *Practice of Clinical Echocardiography.* Elsevier Health Sciences, 1 edition, 2012.

[10] MD Healthline Editorial Team, Medically Reviewed by Steven Kim. Abdominal ultrasound uses. http://www.healthline.com/health/abdominal-ultrasound#Uses2, 2015. Accessed: 2016-05-30.

[11] Wendelken M.E., Markowitz L., Patel M., and Alvarez O.M. Objective, noninvasive wound assessment using b-mode ultrasonography. *Wounds.*, 15, 2003.

[12] von Ramm O. and Smith S. Three-dimensional imaging system. http://worldwide.espacenet.com/publicationDetails/biblio?CC=US&NR=4694434&KC=&FT=E&locale=en_EP, 1987. Accessed: 2016-05-30.

[13] Vscan dual probe. http://www3.gehealthcare.com/en/products/categories/ultrasound/vscan_portfolio/vscan_with_dual_probe, 2016. Accessed: 2016-06-02.

[14] Lerner R.M., Parker K.J., Holen J., Gramiak R., and Waag R.C. Sono-elasticity: medical elasticity images derived from ultrasound signals in mechanically vibrated targets. *Acoust Imaging*, 16:317–327, 1988.

[15] Ophir J., Céspedes I., Ponnekanti H., Yazdi Y., and Li X. Elastography: a quantitative method for imaging the elasticity of biological tissues. *Ultrason Imaging.*, 13:111–134, 1991.

[16] Garra B.S. Elastography: history, principles, and technique comparison. *Abdom Imaging.*, 40:680–697, 2015.

[17] Logiq e9 with xdclear. http://www3.gehealthcare.com/en/products/categories/ultrasound/logiq/logiq_e9#tabs/tabB5A5A24BC9354A1CB0B33E89C7FB4197, 2016. Accessed: 2016-06-07.

[18] Ultrasound elastography. http://www.healthcare.siemens.com/ultrasound/advanced-applications/ultrasound-elastography-systems, 2016. Accessed: 2016-06-07.

[19] Shear wave elastography. http://www.usa.philips.com/healthcare/resources/feature-detail/shear-wave-elastography, 2016. Accessed: 2016-06-07.

[20] Aixplorer | technology. http://www.supersonicimagine.com/Aixplorer-R/Technology, 2016. Accessed: 2016-06-07.

[21] Song P., Urban M.W., Manduca A., Zhao H., Greenleaf J.F., and Chen S. Comb-push ultrasound shear elastography (cuse) with various ultrasound push beams. *IEEE Trans Med Imaging.*, 32:1435–47, 2013.

[22] Ge healthcare - whitepaper logiq-e9 shear-wave. http://www3.gehealthcare.com/~/media/documents/us-global/products/ultrasound/white%20papers/logiq/gehealthcare-whitepaper_logiq-e9%20shear-wave.pdf?Parent=%7B293CA835-658A-4696-B15A-EACCB7E4237B%7D, 2016. Accessed: 2016-06-07.

[23] Tanter M., Bercoff J., Athanasiou A., Deffieux T., Gennisson J.L., Montaldo G., Muller M., Tardivon A., and Fink M. Quantitative assessment of breast lesion viscoelasticity: Initial clinical results using supersonic shear imaging. *Ultrasound Med Biol*, 34:1373–1386, 2008.

[24] Deffieux T., Montaldo G., Tanter M., and Fink M. Shear wave spectroscopy for in vivo quantification of human soft tissues visco-elasticity. *IEEE Trans Med Imaging*, 28:313–322, 2009.

[25] Muller M., Gennisson J.L., Deffieux T., Tanter M., and Fink M. Quantitative viscoelasticity mapping of human liver using supersonic shear imaging: preliminary in vivo feasability study. *Ultrasound Med Biol*, 35:219–229, 2009.

[26] Sandrin L., Fourquet B., Hasquenoph J.M., Yon S., Fournier C., Mal F., Christidis C., Ziol M., Poulet B., Kazemi F., Beaugrand M., and Palau R. Transient elastography: a new noninvasive method for assessment of hepatic fibrosis. *Ultrasound Med Biol.*, 29:1705–1713, 2003.

[27] Gennisson J.L., Lerouge S., and Cloutier G. Assessment by transient elastography of the viscoelastic properties of blood during clotting. *Ultrasound Med Biol.*, 32:1529–1537, 2006.

[28] Catheline S., Gennisson J.L., Delon G., Fink M., Sinkus R., Abouelkaram S., and Culioli J. Measurement of viscoelastic properties of homogeneous soft solid using transient elastography: an inverse problem approach. *J Acoust Soc Am*, 116:3734–41, 2004.

[29] Bercoff J., Chaffai S., Tanter M., Sandrin L., Catheline S., Fink M., Gennisson J.L., and Meunier M. In vivo breast tumor detection using transient elastography. *Ultrasound Med Biol.*, 29:1387–96, 2003.

[30] Fatemi M., Wold L.E., Alizad A., and Greenleaf J.F. Vibro-acoustic tissue mammography. *IEEE Trans.Med. Imaging*, 21:1–8, 2002.

[31] Alizad A., Fatemi M., Wold L.E., and Greenleaf J.F. Performance of vibro-acoustography in detecting microcalcifications in excised human breast tissue: a study of 74 tissue samples. *IEEE Trans. Med.Imaging*, 23:307–312, 2004.

[32] Alizad A., Whaley D.H., Greenleaf J.F., and Fatemi M. Potential applications of vibro-acoustography in breast imaging. *Technol. Cancer Res. Treat.*, 4, 2005.

[33] Alizad A., Whaley D.H., Greenleaf J.F., and Fatemi M. Critical issues in breast imaging by vibro-acoustography. *Ultrasonics.*, 44, 2006.

[34] Hosseini H.G., Alizad A., and Fatemi M. Integration of vibro-acoustography imaging modality with the traditional mammography. *Int. J. Biomed. Imaging.*, 2007, 2007.

[35] Ledoux A. Theory of piezoelectric materials and their applications in civil engineering. Master's thesis, Massachussets Institute of Technology, USA, 2011.

[36] Thieme G.A. Shung K.K. *Ultrasonic Scattering in Biological Tissues.* CRC Press, 11 edition, 1992.

[37] Toronto Western Hospital. Ultrasound for regional anesthesia. http://usra.ca/echoreflection.php, 2016. Accessed: 2016-05-25.

[38] Gennisson J.-L., Deffieux T., Fink M., and Tanter M. Ultrasound elastography: Principles and techniques. *Diagnostic and Interventional Imaging*, 94:487–495, 2013.

[39] Encyclopaedia Britannica. shear modulus. http://global.britannica.com/science/shear-modulus, 2016. Accessed: 2016-05-22.

[40] Daniel A. Russell. Acoustics and vibration animations. http://www.acs.psu.edu/drussell/Demos/waves/wavemotion.html, 2016. Accessed: 2016-06-05.

[41] Sandrin L., Catheline S., Tanter M., Hennequin X., and Fink M. Time-resolved pulsed elastography with ultrafast ultrasonic imaging. *Ultrasonic Imaging*, 21:259–272, 1999.

[42] Young H.D., Freedman R.A., and Ford A.L. *University Physics with Modern Physics*. Addison-Wesley, 13 edition, 2011.

[43] Kasai C., Namekawa K., Koyano A., and Omoto R. Real-time two-dimensional blood flow imaging using an autocorrelation technique. *IEEE Transactions on Sonics and Ultrasonics*, 32:458–464, 1985.

[44] Jhamb T.K., Rejathalal V., and Govindan V.K. A review on image reconstruction through mri k-space data. *I.J. Image, Graphics and Signal Processing.*, 7:42–59, 2015.

[45] Hergum T., Langeland S., Remme E.W., and Torp H. Fast ultrasound imaging simulation in k-space. *IEEE Transactions on Ultrasonics, Ferroelectrics, and Frequency Control*, 56:1159 – 1167, 2009.

[46] Fromageau J., Gennisson J.-L., Schmitt C., Maurice R.L., Mongrain R., and Cloutier G. Estimation of polyvinyl alcohol cryogel mechanical properties with four ultrasound elastography methods and comparison with gold standard testings. *IEEE Trans Ultrason Ferroelectr Freq Control.*, 54:498–509, 2007.

[47] Xia W., Piras D., Heijblom M., Steenbergen W., van Leeuwen T. G., and Manohar S. Poly(vinyl alcohol) gels as photoacoustic breast phantoms revisited. *J. Biomed Opt*, 16, 2011.